Bille, Harner, Loesel

New Frontiers in Vision and Aberration-Free Refractive Surgery

Springer-Verlag
Berlin Heidelberg New York
Barcelona Hong Kong London
Milan Paris Singapore Tokyo

Preface

In recent years, new surgical techniques have evolved for customized correction of refractive disorders, based on groundbreaking achievements in objective assessment of refractive properties of the human eye and greatly refined excimer laser surgical vision correction systems. This book comprises a thorough discussion of the underlying optical and laser-technological principles as well as the first clinical studies for Wavefront-guided LASIK-ablations.

In the first two chapters, the development of wavefront technology and its application to ophthalmology and the assessment of the quality of the human eye are presented. In the following chapters 3 and 4 first clinical results with WaveScan^{TM} in American and European clinics are summarized. The basic technologies, three-dimensional eye-tracking and wavefront-driven custom ablation procedures are covered in chapter 5 and 6. First clinical results of wavefront-driven custom ablation, the so called Heidelberg Study are summarized in chapter 7. In chapter 8 the state of the art in photorefractive keratectomy and LASEK clinical results is presented. Chapter 9 contains with first surgical applications of ultra-short pulse femtosecond laser surgery a glimpse into one of the promising future technological developments in refractive surgery. In Appendix A several contributions of the Refractive Society Symposium(New Orleans, November 11, 2001) are briefly summarized. The book is concluded with Appendix B: *Refractive Outcomes With "One Step" Wavefront-Guided LASIK* with was presented the recent ASCRS-Conference in Philadelphia(June 2002), summarizing the status of the clinical VISX US-FDA study on custom ablations.

On the front cover of the book an artist view of the custom ablation vision correction procedure is illustrated. On the back cover a painting of the Heidelberg Castle is presented. Most of the underlying technologies in wavefront measurements and adaptive optics were developed in the early 1980s at the University of Heidelberg. In addition, the first international clinical study of Wavefront-guided LASIK-Ablation was performed at the surgical eye center("Augenpraxisklinik") in Heidelberg.

The editors are grateful to the authors of this book who have made this multifacetted overview on basic science and engineering as well as surgical and clinical topics possible. It was our intend to provide the refractive sur-

gical community with the most recent results in Wavefront-guided LASIK-Ablations.

The editors are grateful to the editorial group at Springer, Heidelberg for their strong support and are especially indebted to Michael Schottner, M.S. whose considerable editorial skills and excellent computer professionalism was invaluable to the creation of this book, although Dr. Meng Han contributed greatly to finalize the format of the book.

Heidelberg and Santa Clara,
August 2002

J.F. Bille
C. F.H. Harner
F. Loesel

About the Editors

Josef F. Bille, PhD

Josef F. Bille, PhD received the Ph.D. degree from Karlsruhe University, Germany, in 1970. From 1970 to 1974, he was an Assistant Professor at the Institute for Applied Physics of Karlsruhe University, Germany, and from 1974 to 1978, he did research at Hoechst AG,Frankfurt, Germany. Since 1978 , he has been a full professor at the Kirchhoff Institute for Physics, Heidelberg University, Germany. He has been a Guest Professor at the Ecole Polytechnique, Lausanne, Switzerland, at the Optical Sciences Center, University of Arizona, Tucson, and at the Department of Ophthalmology, University of California, San Diego. His research interests include biomedical optics and the development and therapeutical application of medical lasers.

Carol F.H. Harner, PhD

Carol F.H. Harner earned her B.S. and PhD-degrees in Physics at UK-and-US-Universities respectively. After an academic career as a physics professor in Biophysics, she worked in R&D-positions at various companies mainly in the field of cornea-shield biophysiological developments. Since 1999, she the Vice-president of Research&Development with VISX Inc. at Santa Clara, Cal.. Dr. Harner is responsible for the VISX-Custom-Ablation R&D-program and related clinical studies.

Frieder H. Loesel, PhD

Frieder H.Loesel received the Diploma in Physics and the Ph.D. in physics from the University of Heidelberg in 1992 and 1995, respectively. He worked as a scientist at UC Irvine, ETH Zürich, and the University of Michigan. Currently, he is serving as chief executive officer of 20/10 PERFECT VISION, Heidelberg, Germany. Dr. Loesel has published numerous papers on fundamental aspects of laser-tissue interactions and development and application of medical ultrashort pulsed laser systems. Dr. Loesel is a member of several national and international societies for ophthalmology and physics

Addresses of the editors

Prof. Dr. Josef F. Bille

Kirchhoff Institute of Physics
University of Heidelberg
Im Neuenheimer Feld 227
69120 Heidelberg
Germany

Carol F.H. Harner, PhD

VISX,Incorporated
3400 Central Expressway
Santa Clara, CA 95051
USA

Dr. Frieder Loesel

20/10 Perfect Vision
Optische Geräte GmbH
Im Taubenfeld 21-1
69123 Heidelberg
Germany

Contents

List of Contributors

Josef Bille
Kirchhoff Institute of Physics
University of Heidelberg
Im Neuenheimer Feld 227
69120 Heidelberg
Germany

Lorne Bechtel
VISX,Incorporated 3400
Central Expressway
Santa Clara, CA 95051
USA

Joana Büchler
Kirchhoff Institute of Physics
University of Heidelberg
Im Neuenheimer Feld 227
69120 Heidelberg
Germany

Beth Curtrer
VISX,Incorporated
3400 Central Expressway
Santa Clara, CA 95051
USA

John Doane
Discover Vision Center
4741 South Cochise Drive
Kansas City, Missouri 64055
U.S.A

Axel Gleibs
Augenpraxisklinik Heidelberg
Bergheimerstrasse 10-12
D-69115 Heidelberg
Germany

Erik Gross
VISX,Incorporated
3400 Central Expressway
Santa Clara, CA 95051
USA

Carol F.H. Harner
VISX,Incorporated
3400 Central Expressway
Santa Clara, CA 95051
USA

W. Bruce Jackson
University of Ottawa Eye Institute
501 Smyth Road Ottawa
Ontario, Canada K1H 8L6

Ralf Kesseler
20/10 Perfect Vision
Optische Geräte GmbH
Im Taubenfeld 21-1
69123 Heidelberg
Germany

Douglas D. Koch
Cullen Eye Institute
Baylor College of Medicine
6565 Fannin, NC-205
Houston, TX 77030
USA

Colman Kraff
Kraff Eye Institute
25 East Washington, Suite 606
Chicago, IL 60602
USA

Frieder Loesel
20/10 Perfect Vision
Optische Geräte GmbH
Im Taubenfeld 21-1
69123 Heidelberg
Germany

Robert K. Maloney
Maloney-Seibel Vision Institute
10921 Wilshire Blvd., Ste. 900
Los Angeles, CA 90024
USA

Frank Müller
Kirchhoff Institute of Physics
University of Heidelberg
Im Neuenheimer Feld 227
69120 Heidelberg
Germany

Terrence O'Brien
Wilmer Ophthalmological Institute
Woods 225
The Johns Hopkins Hospital
601 N. Broadway
Baltimore, MD 21287-9121
USA

Ulrich von Pape
20/10 Perfect Vision
Optische Geräte GmbH
Im Taubenfeld 21-1
69123 Heidelberg
Germany

John Shimmick
VISX,Incorporated
3400 Central Expressway
Santa Clara, CA 95051
USA

Gustavo Tamayo Bogota Laser
Refractive Institute
Calle 114#9-45
Torre Bonite 718
Bogota, Columbia

Rainer Volz
Augenpraxisklinik Heidelberg
Bergheimerstrasse 10-12
D-69115 Heidelberg
Germany

Jason Watson
VISX,Incorporated
3400 Central Expressway
Santa Clara, CA 95051
USA

Jonathan Wong
VISX,Incorporated
3400 Central Expressway
Santa Clara, CA 95051
USA

Kingman Yee
VISX,Incorporated
3400 Central Expressway
Santa Clara, CA 95051
USA

Leander Zickler
Kirchhoff Institute of Physics
University of Heidelberg
Im Neuenheimer Feld 227
69120 Heidelberg
Germany

1 The Development of Wavefront Technology and Its Application to Ophthalmology

J.F. Bille

1.1 Abstract

Wavefront-technology was originally developed for the improvement of star images in optical astronomy. In 1978, this technology was for the first time applied to ophthalmology. At the University of Heidelberg, Germany, a closed loop adaptive-optical system was designed to compensate for optical aberrations of the human eye. In the meantime, superresolution in retinal imaging has been achieved, providing detailed information on photoreceptors, small blood vessels and nerve fibre structure in the human eye in vivo. Recently, new wavefront technology has been developed for the assessment of the human eye and it is now possible to apply a custom treatment to the eye, using the excimer laser. An adaptive optical closed loop system has been devised for preoperative simulation of refractive outcomes of aberration-free refractive surgical procedures. Treatment of a patient's entire wavefront error has been demonstrated to improve the patient's visual acuity beyond best-spectacle corrected vision.

1.2 Introduction

Wavefront technology was originally developed nearly fifty years ago for astronomical applications. It was used to measure wavefront distortions that occurred when light travelling through the atmosphere entered an optical telescope. By applying adaptive optical closed loop controls the speckle patterns of the star images could be improved towards diffraction-limited performance. Most of the technology was developed in association with research towards anti-missile-defence systems in the late nineteen-hundredseventies.

Historically, refractive errors of the human eye were corrected by glasses or contact lenses or more recently eximer-laser-surgery: but such corrections were limited to the compensation of myopia, hyperopia, or regular astigmatism. Indeed the optical system of the human eye as a genuine optical system generates more complex distortions to the retinal images, the so-called higher order aberrations. These aberrations are unique for the very particular eye of the patient. Under daylight vision conditions the pupil of the human eye is small, e.g. 2-3 mm diameter. so that the light travels essentially along the

optical axis of the human eye (Fig. 1.1). Under these conditions higher order aberrations are limited so that a sharp retinal image is formed. Under twilight vision conditions the pupil of the human eye dilates to approx. 5-7 mm diameter resulting in increased importance of higher order aberrations. (Fig. 1.2). These higher order aberrations result in considerable distortions to the retinal image as a considerable part of the light is transmitted through marginal areas of the human eye, away from the optical axis. These image distortions impair the visual acuity even in patients with normal vision (20/20 visual acuity) considerably.

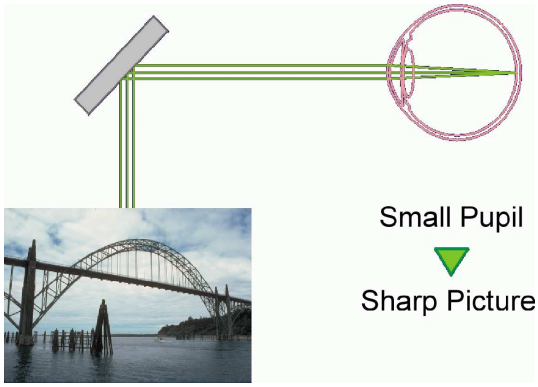

Fig. 1.1. Daylight Vision

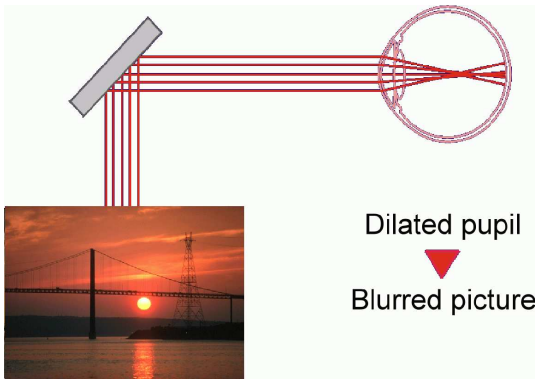

Fig. 1.2. Twilight Vision

These complex distortions can now be assessed with the newly developed wavefront technology (Fig. 1.3). The image quality in front of the human eye is described by the green regular mesh of lines, the reduced image quality af-

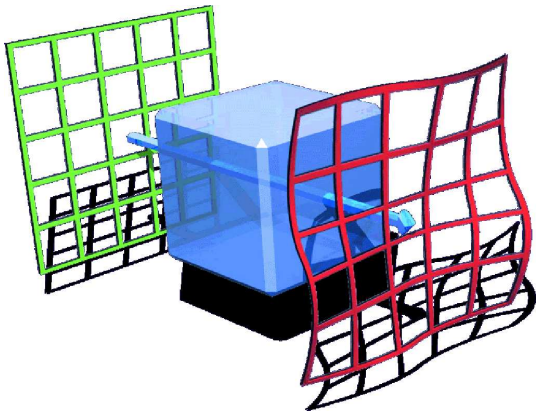

Fig. 1.3. Description of optical imaging system

ter transmission through the optical system of the human eye is exemplified by the distorted red mesh of lines. In recent years different wavefront sensors based on a number of principles have been developed, the most important ones being Tscherning-Ray-Tracing and Shack-Hartmann-Sensors. Recently the application of wavefront sensing for pre-operative evaluation of refractive surgical procedures has been proposed. Adaptive optical closed loop systems can be used to subjectively measure and compensate the higher order optical aberrations of the human eye to guide the surgeon in selection of the parameters of the procedure.

1.3 History

Starting in 1978, the principle of wavefront measurement and compensation was adapted at the University of Heidelberg for ophthalmic applications. The technique is based an Shack-Hartmann-Sensing, measuring the optical path of light rays through the eye to detect all aberrations at all point in the optical system of the human eye. Adaptive optical systems were developed which measure and compensate wave aberrations of the human eye with closed loop control [1,2].

As early as 1982 [1] at the 6th Int. Conference on Pattern Recognition in Munich, Germany wavefront sensing and adaptive optical closed loop control was proposed for aberration free imaging and vision testing: “The system essentially provides an elimination of optical eye aberrations which diminish the fundus image quality. On the other hand by active focus control and/or wavefront sensing the aberrations of the human eye like astigmatism of the cornea and spherical aberration of the lens can be measured.” (Last paragraph in [1]). In another publication [2] the concept of achieving 20/10 visual acuity by adaptive optical visual stimulus generation was described: “In the apparatus of this invention the illuminating laser beam is generally widened to a

diameter of between 3 mm and 4 mm, in exceptional cases even still wider, and by compensation for all existing aberrations it is possible to focus the laser beam on a spot of a minimal diameter between 2 and 3 micrometers on the retina. This permits the resolution of more than 5000 image points per scan line, that is, it is possible for example to resolve and represent individual receptors in the fovea. Since the use of optical image focussing under adaptive control produces data on the wavefront of the imaging laser beam, the apparatus of this invention enables the refractive index profile within the eye to be reconstructed, permitting for the first time an automatic determination of the refraction at high accuracy." (column 4 lines 1-16 from [2]).

At the same time an adaptive optical control system was devised and built which was based on modal actuator control (Fig. 1.4). In a modal phase compensation, the wavefront aberration is expanded into orthonormal expansion system which was based on Zernicke Polynomials. In addition, the original concept included a Karhunen-Loève-wave expansion, in order to account for partial wavefront distortions with high spatial frequency content [3].

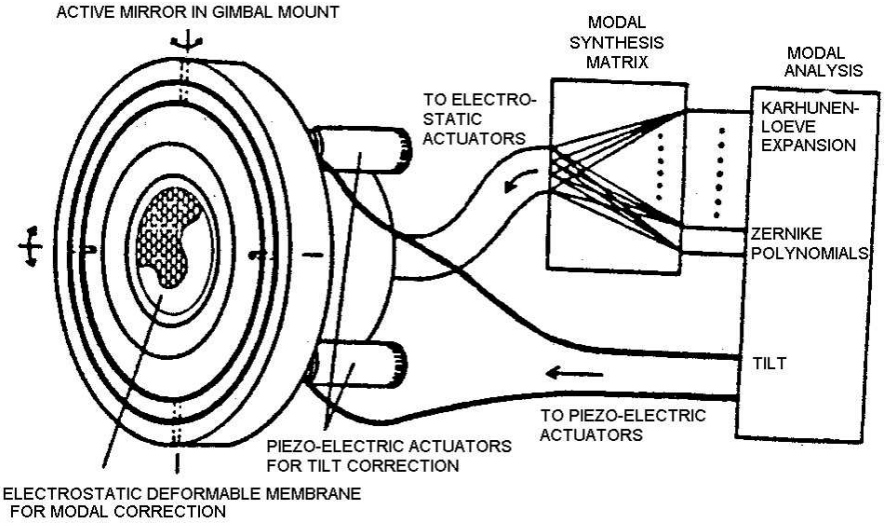

Fig. 1.4. Closed Loop adaptive-optical system with modal actuator (from [3]) control

1.4 Principle of Aberration Measurement

In recent years, basically 3 types of aberration measurement devices have been developed: The thinbeam-Raytracing-Aberrometer, the Tscherning-Aberrometer, and the Shack-Hartmann-Method. In Fig. 1.5, the principle of operation of the Shack-Hartmann-Wavefront-Sensor is demonstrated. On the left

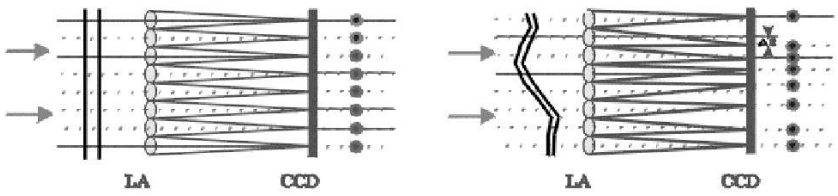

Fig. 1.5. (Left): Incident plane wave resulting in a square grid of spots. (Right): Distorted wavefront causes lateral displacement of spots

hand side the processing of an ideal plane wave is depicted. The incident plane wave results in a square grid of spots in the focal plane of the micro lens array. On the right hand side, the imaging of a distorted wave is shown. The distorted wavefront causes lateral displacements of the spots on the CCD-array. From the spot pattern the shape of the incident wavefront can be reconstructed based on appropriate curve fitting algorithms. More than ten years ago the first detailed study of the application of wavefront technology for the assessment of the refractive properties of the human eye was performed. From the wavefront measurements Zernicke Coefficients were calculated and the wavefronts emerging from the eyes tested were reconstructed. Fig. 1.6 shows the equal level contour maps of a human eye [4–6]. On the left hand side of Fig. 1.6 the overall wavefront is presented, whereas in the right hand side only the higher orders, i.e. the 3rd- and 4th-order Zernicke Coefficients are depicted. In this work, the phase error that can not be corrected by conventional spectacles was specified as the high order aberrations of the eye. In

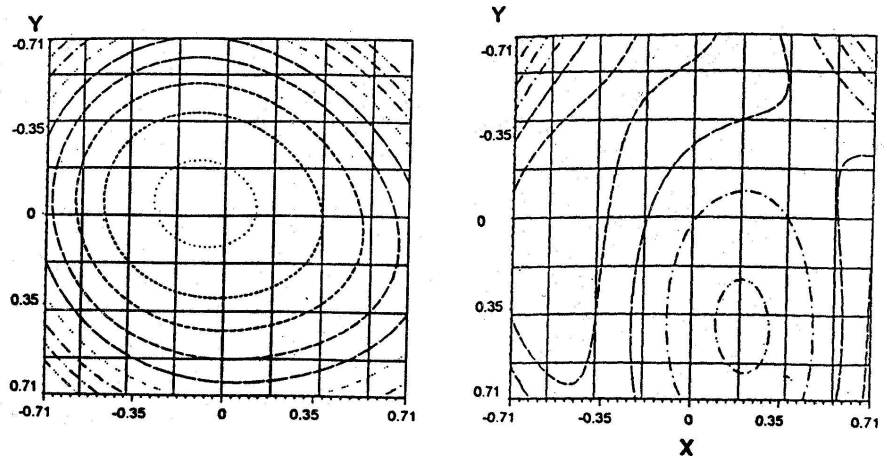

Fig. 1.6. Equal level contour map of a human eye (from [6]). Overall wavefront (left hand side), higher orders (3rd- and 4th-order Zernikes, right hand side)

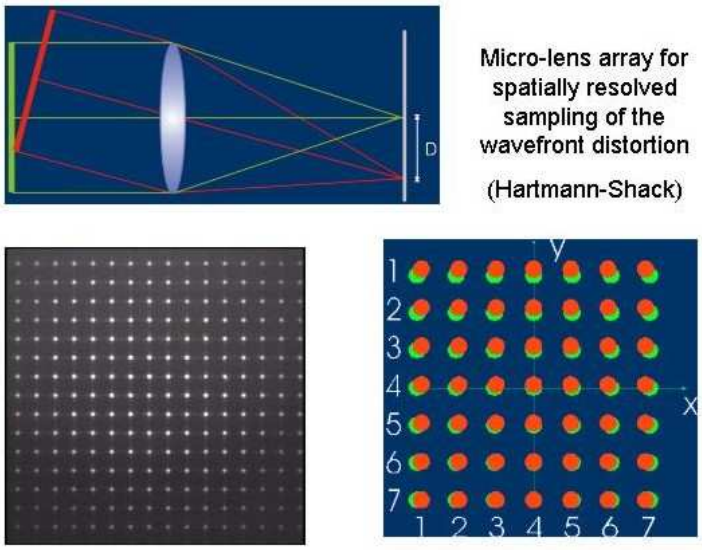

Fig. 1.7. Principle of Wavescan^{TM} measurements

Fig. 1.7 the principle of the measuring process of the Wavescan^{TM}instrument is shown. The ideal wavefront is represented as a regular grid of spots coded with green color. The distorted wavefront is given by an irregular grid of spots coded with red color, resp. blue color. In Fig. 1.8 the computer display of the WaveScan^{TM} instrument is presented summarizing the measurement results for the right (OD) and left (OS) of a human volunteer subject. In the upper part of the display the AcuityMap^{TM}'s for both eyes are depicted in a color coded form. In the lower part of the display ("Bille Aberration Map^{TM}") the higher orders of the optical aberrations beyond sphere and cylinder are plotted demonstrating considerable wavefront deviations in the outer segments of the pupil, i.e. coma and spherical aberration respectively. In addition, optical performance indices like RMS or OAI are given.

1.5 Definitions of Optical Imaging Quality

For the description of the performance of an optical system there are several parameters in use. Some of them are applied to the human eye as well. A short overview of some scales used in ophthalmology will be given in this section.

Root Mean Square

The RMS of the wavefront is a very simple criterion. It is nothing but the integrated root mean square of the differences between the wavefront surface

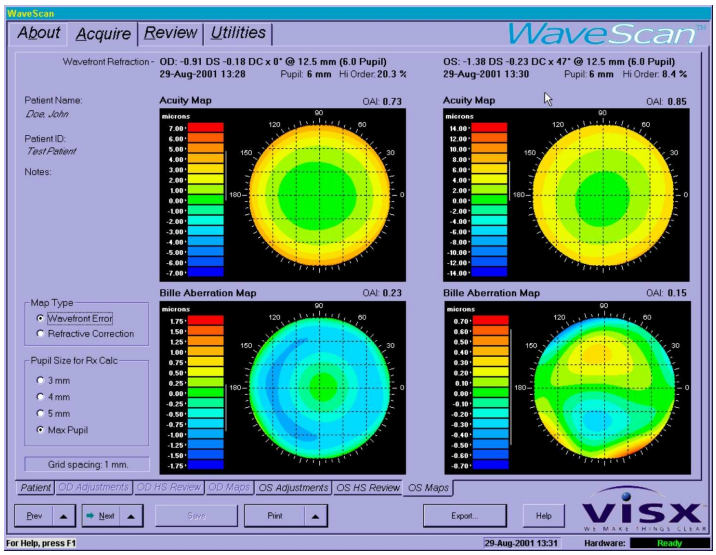

Fig. 1.8. Computer display of Wavescan$^{\mathrm{TM}}$-instrument

and the mean value of the surface. The complex phenomenon of aberration is packed into a single number. This makes it so convenient in ophthalmology. The RMS can be calculated directly from the Zernike polynomials.

For the calculation of the RMS we refer to Zernike polynomials of second order minimum. The zero order is not measured at all. The first order gives information about the tilt only, which is connected to the position of the eye. It does not supply any information about the characteristics of the eye itself. The Zernike polynomials are orthogonal and the zero order term is set to zero. So the mean value of the wavefront surface is zero, too. The RMS is thus simply the mean squared value of the wavefront over the pupil.

$$\mathrm{RMS} = \sqrt{\frac{\int_0^r \int_0^{2\pi} W(\rho,\theta)^2 \rho d\rho d\theta}{\int_0^1 \int_0^{2\pi} \rho d\rho d\theta}} = \sqrt{\frac{1}{\pi}\int_0^1 \int_0^{2\pi} W(\rho,\theta)^2 \rho d\rho d\theta} \tag{1.1}$$

In taking mean values of the Zernike polynomials the integral can be replaced by a sum of the weighted coefficients. For a real pupil size the integration will be from 0 to r.

$$\mathrm{RMS} = \sqrt{\frac{\int_0^r \int_0^{2\pi} W(\rho,\theta)^2 \rho \, d\rho \, d\theta}{\int_0^r \int_0^{2\pi} \rho \, d\rho \, d\theta}} \tag{1.2}$$

$$= \sqrt{\frac{1}{\pi r^2}\int_0^r \int_0^{2\pi} \left(\sum_{i=0}^{\mathrm{order}} c_i Z_i(\rho,\theta)\right)^2 \rho \, d\rho \, d\theta} \tag{1.3}$$

$$= \sqrt{\frac{1}{\pi r^2} \sum_{i=0}^{\text{order}} c_i^2 \int_0^{2\pi} \int_0^1 Z_i^2(\rho,\theta)\rho \, d\rho \, d\theta} \tag{1.4}$$

$$= \sqrt{\frac{1}{\pi r^2} \sum_{i=0}^{\text{order}} c_i^2 {Z'}_i^2} \tag{1.5}$$

with Z'_i = weighting coefficient for each Zernike. It depends from the radial and angular order.

$$Z'_i = \frac{1}{(2-\delta_l) * (n+1)} \quad \text{with} \quad i = \frac{n(n+1)}{2} + \frac{n-l}{2} + 1 \tag{1.6}$$

With 3.21 the RMS can be calculated simply as a root of the sum of coefficients. This makes calculations with the RMS very easy.
The Peak To Valley (PTV) is closely connected to the RMS. While the PTV depends – heavily – on just two extreme values, the RMS is a kind of mean value received from the complete set of data points. This makes the RMS much more stable against deviations.

Optical Aberration Index

The Optical Aberration Index (OAI) is defined as

$$\text{OAI} = 1 - e^{(-\text{RMS})} \tag{1.7}$$

The OAI has values between zero and one. Zero stands for an optical system that is perfect and 1 for infinite aberrations. The OAI is very sensitive in the typical range for higher order aberrations. It was introduced as an even simpler scale for the optical quality of an eye.

Modulation Transfer Function

A typical target for testing the quality of an optical system consists of a series of alternating black and white bars of equal width with a contrast of 1. These targets are connected to a vision chart with Snellen E's, as used in ophthalmology. The Modulation Transfer Function (MTF) gives the contrast of the image (as percentage of the contrast of the object) in dependence of the frequency. The contrast is defined by:

$$\text{Contrast} = \frac{I_{\max} - I_{\min}}{I_{\max} + I_{\min}} \tag{1.8}$$

The MTF may be compared to the Aerial Image Modulation (AIM) curve. This curve shows the smallest amount of modulation a sensor like a CCD-camera or the retina is able to detect. The AIM is a function of the frequency

used as well. As the MTF normally goes down with frequency increasing, the AIM increases with frequency. The point of intersection gives the resolution. For a diffraction limited optic the MTF can be calculated by

$$\mathrm{MTF}(\nu) = \frac{M_i}{M_o} = \frac{2}{\pi}(\Phi - \cos\Phi \sin\Phi) \tag{1.9}$$

with

$$\begin{aligned} \Phi &= \arccos \frac{\lambda\nu}{2NA} \\ \nu &= \text{frequency in} \frac{\text{cycles}}{\text{mm}} \\ \mathrm{NA} &= \text{numerical aperture} \\ \lambda &= \text{wavelength} \end{aligned}$$

Point Spread Function

The point response of an optic should still be a point. Even if the optic is perfect the response is a pattern - due to the diffraction. In a real system the aberrations widen the image up to a spot. The spot is represented by a 2-dimensional distribution. This is described by the Point Spread Function (PSF).

If the aberrations are smaller than $0.25\,\lambda$ (Rayleigh criterion) the diffraction pattern provides a good description of the PSF.

Up to about $2\,\lambda$ it is appropriate to consider the manner in which the aberration affects the diffraction pattern. For larger wavefront aberrations illumination described by raytracing is sufficient for description.

Application of the Performance Indices in a Normal Human Eye

In Fig. 1.9, the different performance indexes are presented for a normal human eye. In the upper part, a color-coded presentation of the wavefront is shown. The Root Mean Square (RMS) of $0.23\,\mu$m results in an Optical Aberration Index (OAI) of 0.24. In the middle part, the Modulation Transfer Function (MT) is plotted, as well as the diffraction limited MTF for a 6 mm pupil. In the lower part, the Point-Spread-Function (PSF) is graphically presented.

1.6 Principle of Closed Loop Adaptive Optical Control

In Fig. 1.10, the principle of closed loop adaptive optical control is schematically demonstrated. The wavefront of light which is distorted due to optical aberrations of the optical system, e.g. the human eye, is measured by

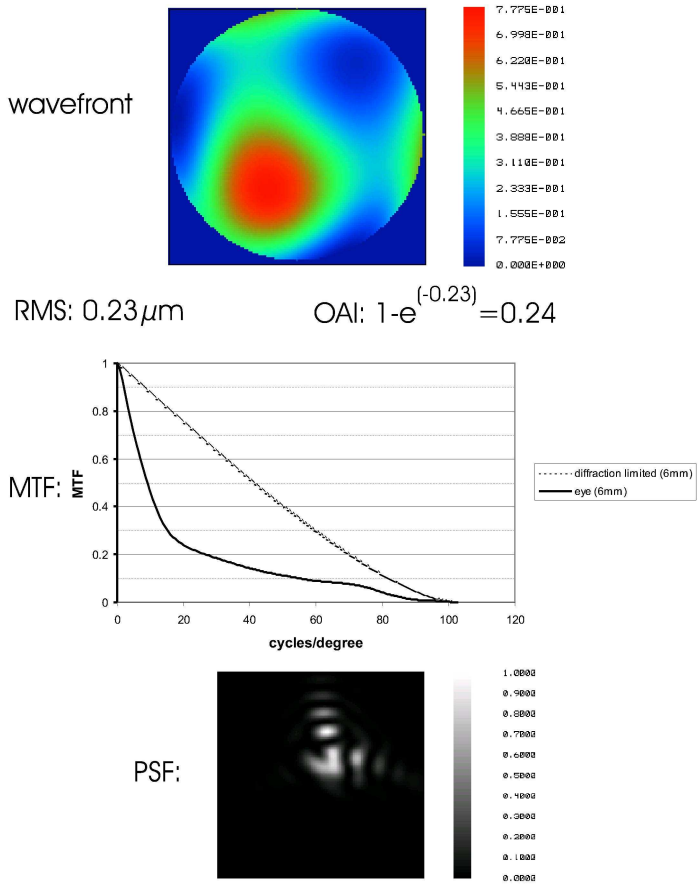

Fig. 1.9. Different representations of the image quality of a human eye

a wavefront sensor. The reconstructed wavefront is dithered on a wavefront controller, e.g. an active mirror in order to compensate for the optical aberrations. Thus, through an aberrating medium an aberration free optical image can be achieved.

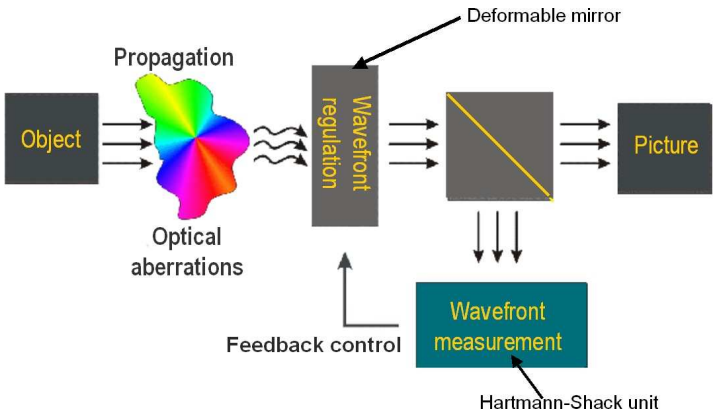

Fig. 1.10. Principle of closed loop adaptive optical control

Adaptive Optics in Astronomy

Wavefront technology and adaptive-optical closed loop control was originally developed for astronomical applications. It was used to measure wavefront distortions that occurred when light travelling through the atmosphere entered an optical telescope. By applying adaptive optical closed loop controls the speckle patterns of the star images could be improved towards diffraction-limited performance. In Fig. 1.11, the principle of operation of an adaptive optical closed loop system on an optical telescope is demonstrated. In the left picture (a) the speckle pattern of an astronomical object, aberrated by the turbulent atmosphere is shown. In the right picture (b) the sharpened picture after engagement of the adaptive optical closed loop control demonstrating a double star image at high spatial resolution is depicted. The measurements where performed at the Calar Alto Optical Telescope operated by the Max Planck Institute for Astronomy, Heidelberg [9].

History of Adaptive Optics at the University of Heidelberg

In Fig. 1.12 a number of active mirrors and wavefront sensors as developed and used in the Kirchhoff Institute of Physics, University of Heidelberg during the last 20 years are depicted. The first generation foil mirror was successfully applied for the real time compensation of aberrations of the human eye for high resolution imaging of the retina [8]. In this paper closed loop operational results of the second generation foil mirror [10] are reported. Recently a multi-segment microchip mirror was developed, exhibiting approximately 100,000 mirror facets, each able to slightly shift the phase of a local component of the wavefront in order to compensate for the detected wavefront error. In the lower part of Fig. 1.12 two different realisations of Hartmann Shack wavefront sensors are shown. On the left hand side a cylindrical lens array with CCD detector is photographed which was applied for the first time to measure

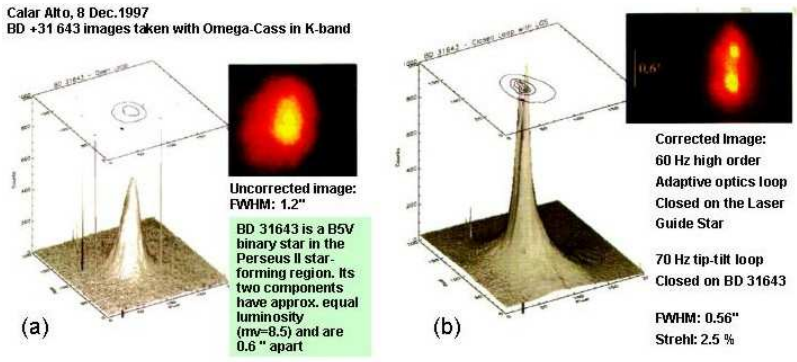

Fig. 1.11. Adaptive Optics in Astronomy: (**a**) speckle pattern (**b**) sharpened picture

the aberration of the human eye in real time [6]. On the right hand side a custom ASIC chip detector which is used in combination with a custom micro lens array is shown [12]. The ASIC chip is divided into a matrix of clusters, consisting of photodetectors and signal processing circuitry. By analogous signal processing in winner-takes-all-circuitry, the highest photocurrent is detected and position is calculated. The data obtained are evaluated in real time for reconstruction of the wavefront of the light.

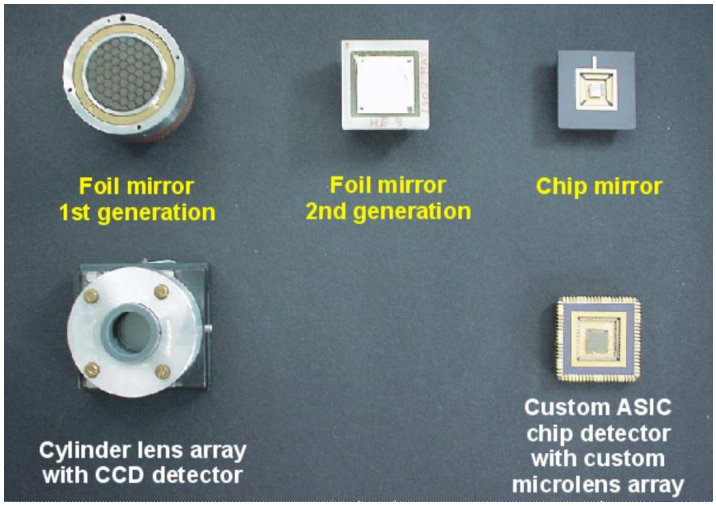

Fig. 1.12. History of adaptive-optical elements

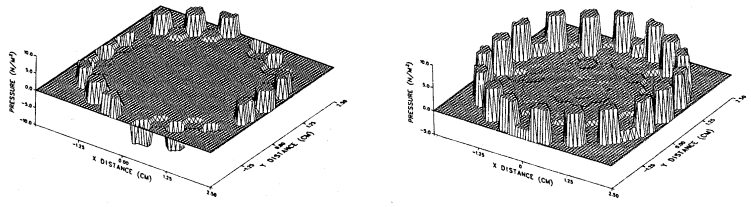

Fig. 1.13. Pressure distribution for Zernike polynomials U_3^3(left part) and U_6^0(right part) (from [7])

Performance of Foil Mirrors

Electrostatic foil mirrors as e.g. introduced at the University of Heidelberg [12] and the University of Delft [10] suffer from the cross talk of influence functions on neighboring sites. In order to accomplish the early work in aberration free imaging of the retina of the human eye (see e.g. [8]) a control system for determining optimal voltage settings for producing a desired foil mirror surface shape was developed [7]. Electrode pressures and voltages where calculated for Zernicke Polynomials up to degree $n = 6$ (see Fig. 1.13).

Two Zernicke polynomials where selected to illustrate the fitting procedure. They are

$$U_3^3 = r^3 \cos 3\Phi \tag{1.10}$$

and

$$U_6^0 = 20r^6 - 30r^4 + 12r^2 - 1 \tag{1.11}$$

computed surface displacements for Zernicke polynomials U_3^3 and U_6^0 are shown in Fig. 1.13 [7]. The difference between the desired and computed surface displacements is caused by the limitations in spatial resolution of both the finite number of electrodes and the finite number of surface-matching points in the algorithm. In the mid-1980s at the University of Heidelberg for the first time the compensation of aberrations of a human eye with an an adaptive-optical system was accomplished [8] using the method of configuring electrostatic membrane mirrors by least squares fitting with analytically derived influence functions, as described previously (see Fig. 1.14).

For an adaptive optical system with a foil mirror as an actuator the performance of closed loop operation was simulated. In Fig. 1.15 the result of a compensation of defocus based on the Gauss-Seidel algorithm is graphically demonstrated. The membrane mirror consists of a silicon nitride membrane coated with aluminum. It is deformed by electrostatic forces of 37 underlying electrodes, arranged in a hexagonal grid [10]. Since the realtime compensation with a closed loop requires, compensation of accommodation, another approach was chosen. A genetic algorithm was used to determine the manifold of voltages that yielded the best compensation.

In Fig. 1.16 two examples of compensation of low order optical aberration using the genetic algorithm are shown. In the upper part of Fig. 1.16 the compensation of defocus is depicted. In the lower part of Fig. 1.16 the compensation of astigmatism has been tried but with lesser success: though the wavefront RMS is decreased to less than one half, the achieved residual RMS of 0.41 μm is far away from diffraction limited imaging. Thus the performance of the foil mirror is not adequate for compensation of higher order optical aberrations of the human eye.

Comparison of Foil Mirrors and Microchip Mirror

Recently, an active matrix mirror was developed exhibiting an array of 200 μm $\times$ 240 μm mirrors (40 μm $\times$ 40 μm each). With this technique wavefronts can be corrected up to twice the height of deflection, i.e. approximately one wavelength. By using the 2-π-phase wrapping method the range of the wavefront deformation to be corrected can be largely enhanced.

In a simulation, the foil mirror and the multi-micro-mirror-system were compared for a compensation of astigmatism of one diopter (Fig. 1.17). On the left side of Fig. 1.17 the simulated vision chart blurred by an astigmatism of 1 diopter is shown. In the middle the vision after correction with a 37 element membrane mirror is depicted. It is obvious that due to the limited resolution a remaining astigmatism of 0.3 diopters yields considerable blur of the smaller Snellen-letters. On the right side of Fig. 1.17 the result of a compensation with the multi-micro-mirror/micro-chip-mirror is presented demonstrating a complete compensation down to the 20/10 letter line.

1.7 CLAO/BILLE-Aberrometer

Historically, for specifying the optical quality of large telescopes, in 1920 Johannes Hartmann introduced a new measuring method, called now the Hartmann Test. In Fig. 1.18 a modern version of the Hartmann Test as applied

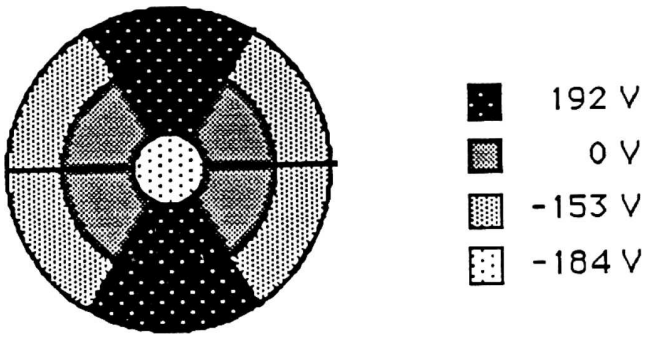

Fig. 1.14. Voltage distribution of foil mirror for astigmatism compensation on human eye (from [8])

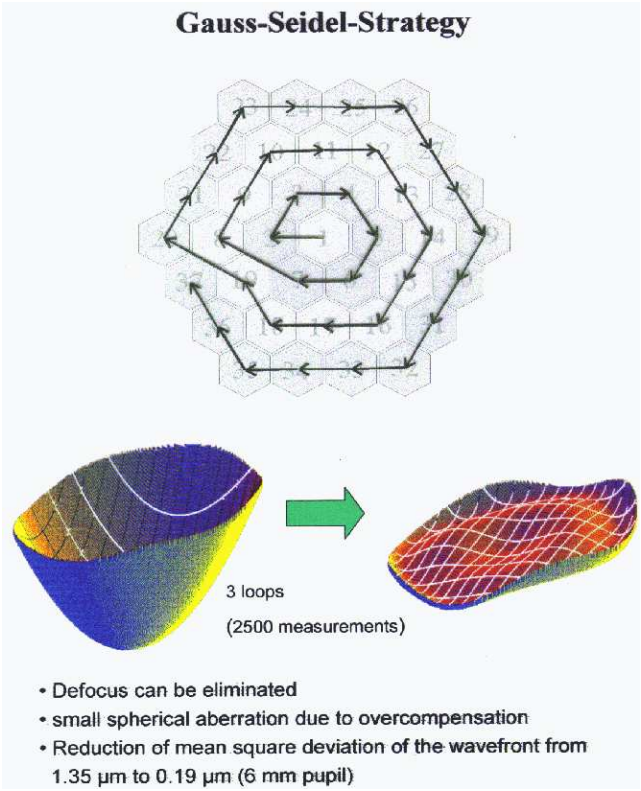

Fig. 1.15. Gauss Seidel Algorithm

to measuring the aberrations of the human eye is schematically diagrammed. The Hartmann Screen is placed in front of a CCD array so that every imaging point can be associated with one aperture. As discussed in chapter 4 the position of the image point encodes the local slope of the wavefront. In 1971 Roland Shack introduced an advanced version of the Hartmann Sensor called the Hartmann Shack sensor (Fig. 1.19). The modification comprises the use of a lens array in the image plane followed by a photographic plate or nowadays a CCD camera in the focal plane of the lens array. The confinement of the individual light race into focal spots on the CCD chip allows for increased signal to noise ratio and thus increased speed of the wavefront measurement. Still the resolution of the measuring device is limited to the size of a single lens in the lens array, typically around 0.5 mm. Recently a new type of a wavefront measuring device has been introduced, the so called Closed Loop Adaptive Optical Aberrometer (CLAO/Bille-Aberrometer, see Fig. 1.20). In the CLAO/BILLE Aberrometer the spatial resolution of the wavefront measurement is limited by the size of the individual mirrors of the micro chip mirror which is typically less than 0.05 mm, thus increasing the

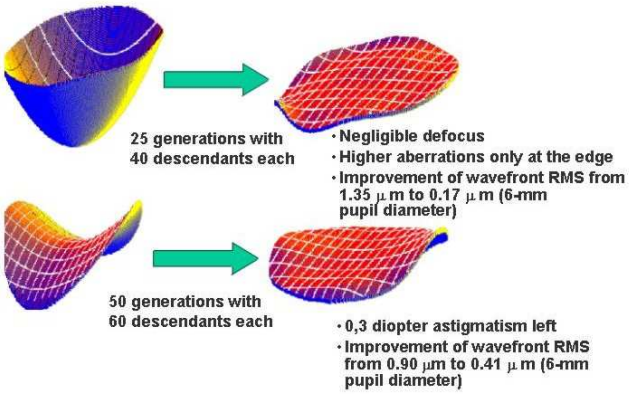

Fig. 1.16. Results Genetic Algorithm

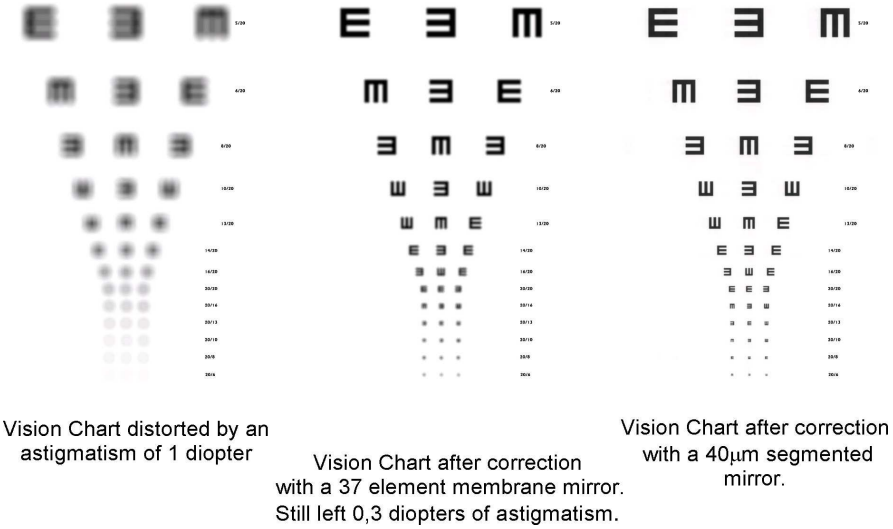

Fig. 1.17. Comparision of mirrors [16]

spatial resolution by a factor of one hundred over typical Hartmann Shack sensors. The lens array/CCD-camera detector is only used as a nulling-sensor for achieving complete compensation of the measured wavefront. In addition, it delivers an initial estimate of the aberrated wavefront. As an alternative to the Hartmann-Shack Sensor as a nulling-sensor a newly developed pyramid sensor is considered (see Fig. 1.21), The wavefront sensor consists of a lens relay and an oscillating, pyramidal-shaped prism. The gain of the device is driven by the amplitude of the oscillations, while the sampling is determined by the focal length of the lens relay.

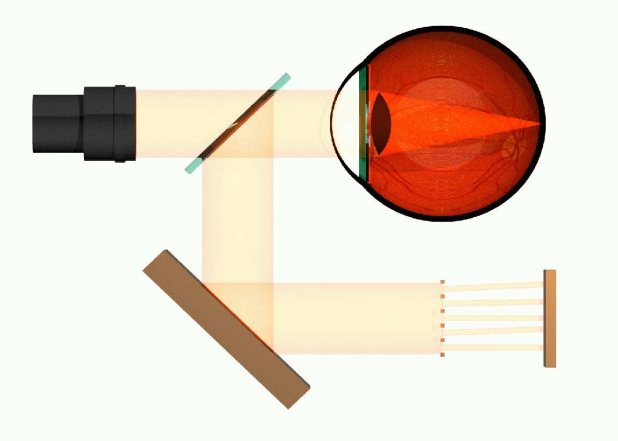

Fig. 1.18. Hartmann test of the aberrations of the human eye

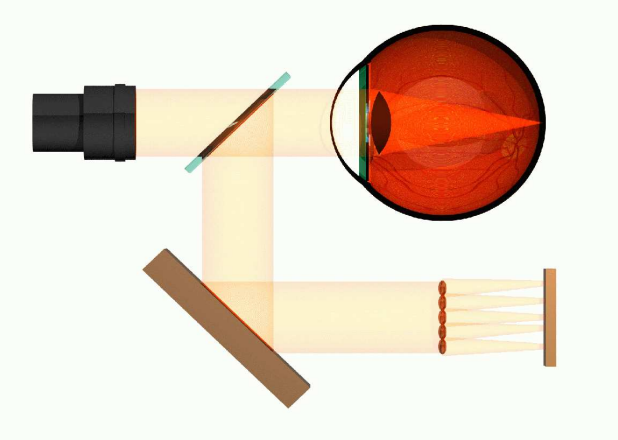

Fig. 1.19. Hartmann-Shack Wavefront sensor

Following the notations of Fig. 1.21, the slope of the wavefront can be calculated. The modulation amplitudes

$$\frac{\partial W}{\partial x}(p) = \delta\Theta_x \frac{(S_1 + S_4) - (S_2 + S_3)}{S_1 + S_2 + S_3 + S_4} \tag{1.12}$$

$$\frac{\partial W}{\partial y}(p) = \delta\Theta_y \frac{S_1 + S_4) - (S_2 + S_3)}{S_1 + S_2 + S_3 + S_4} \tag{1.13}$$

determine the optical gain. As an advantage over the Hartmann-Shack Sensor the pyramid wavefront sensor yields a higher sensitivity in closed loop application [15].

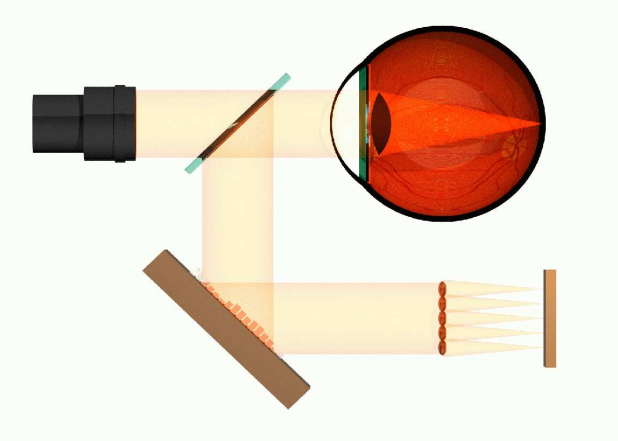

Fig. 1.20. CLAO/BILLE-Aberrometer

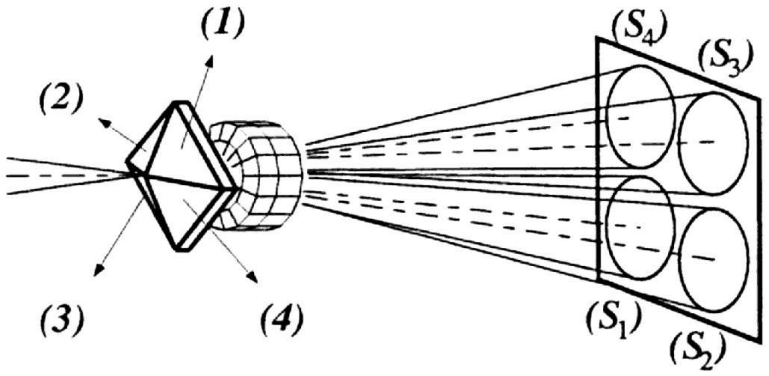

Fig. 1.21. Pyramid wavefront sensor

In Fig. 1.22 an experimental realisation of the closed loop adaptive optical aberrometer is schematically shown [14]. There are four main parts in the optical path, two for the measurement itself and two for the accurate positioning of the eye. To prevent interferences between the parts, each part uses light beams with special wavelengths or polarisations optimized for the particular use (Fig. 1.22, top). In order to measure ametropic eyes a spherocylindrical compensator is incorporated (Fig. 1.22 bottom). A telescopic arrangement is used to compensate the measuring beam for defocus. Behind the second lens of the anterior telescope a cylinder compensation unit is introduced, consisting of two rotatable cylinder lenses with focal lengths identical in amount, but opposite in sign.

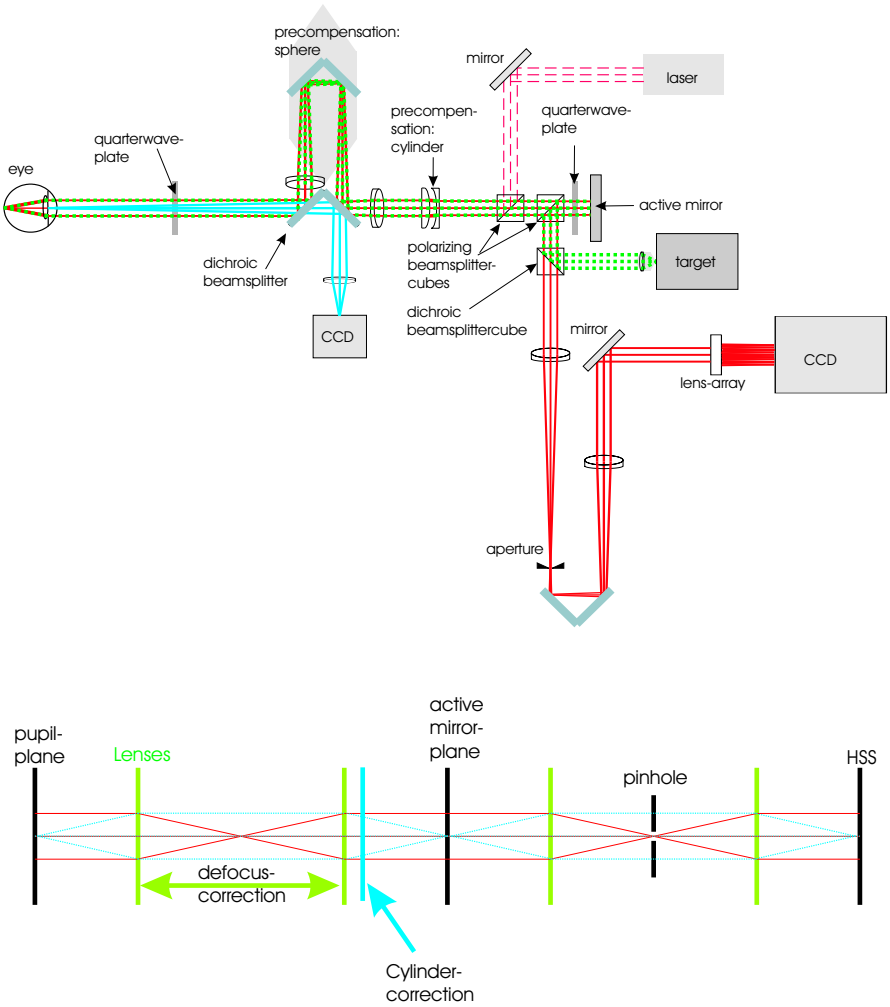

Fig. 1.22. Setup of CLAO/BILLE-Aberrometer

1.8 Demonstration of CLAO/BILLE-Aberrometer

An active matrix mirror is used in the device (see Fig. 1.23). It is an array of 200×240 micromirrors ($40\,\mu\text{m} \times 40\,\mu\text{m}$ each). Each one of the mirrors can be lowered up to 400 μm independently. The mirrors can only be lowered without the facility of tilting. With this technique wavefronts can be corrected up to the double height of deflection - more than one wavelength. By using the 2-π-phase wrapping method (Fig. 1.24) the range of the wavefront deformations to be corrected can be enlarged by far. The 2-π method makes use of the phase properties of light. A sag of 2-π between two neighboring mirrors has

no effect on the direction of the light and can be subtracted without any effect on the wavefront. So the range of movement needed for the correction of any wavefront-deformation can be reduced to $\lambda/2$. In fact the use of the mirror is limited to light of one wavelength when using the 2-π-phase wrapping method [11].

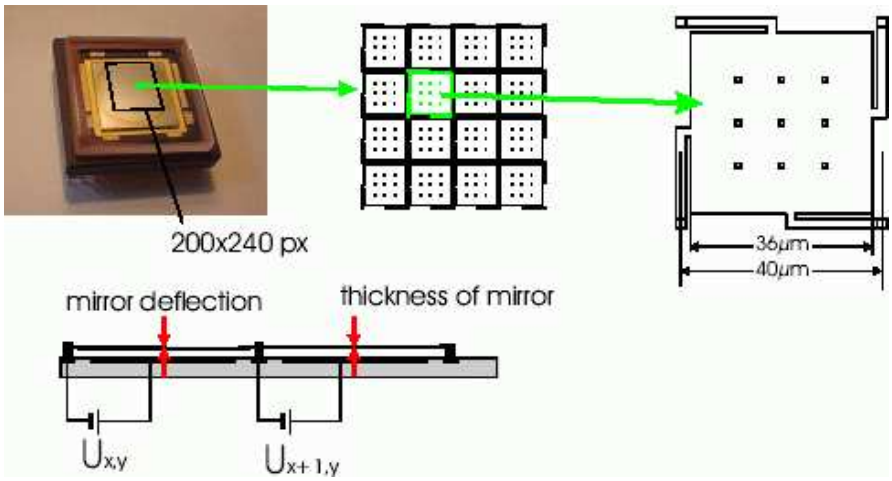

Fig. 1.23. Setup of the microcho-mirror

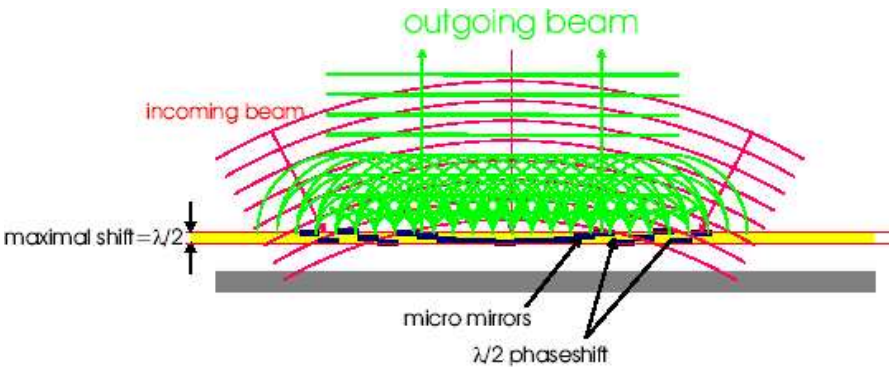

Fig. 1.24. 2π-phase wrapping control of the micromirror

For an objective test of the active mirror a test device was constructed (Fig. 1.25). This device allows us to measure a phase-plate and look through it into the instrument at the same time. By the camera at the test device we get an image of the target. For the measurements presented here, a target was used with $1'$ apex angle corresponding to a VA of 1.0.

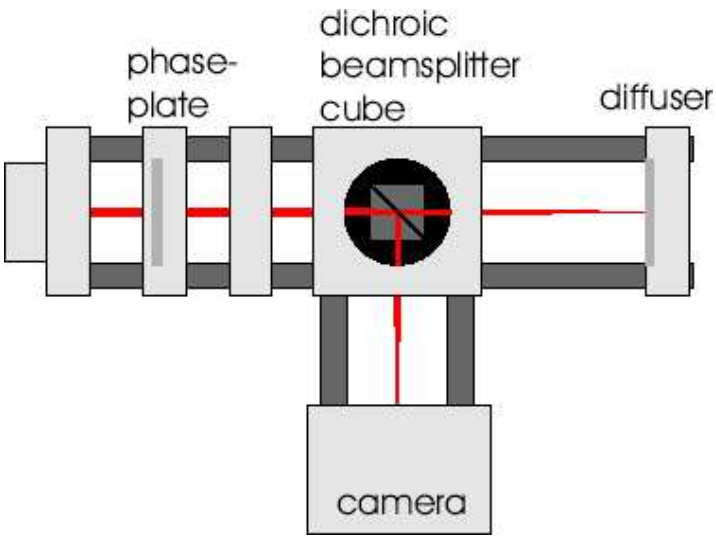

Fig. 1.25. Test device for the active mirror: Light entering from the left through the phase plate is divided by the dichroic beamsplitter cube. The aberrations get measured in the right arm. The bottom arm is used to record an image of the target

In Fig. 1.26 and Fig. 1.27 the correction of higher order wave aberrations is demonstrated. In Fig. 1.26 on the right hand side, the uncompensated coma modelled into a waveplate is shown, resembling the aberration of a human eye before therapeutic custom ablation correction. The peak to valley (PTV) difference amounts to $2\,\mu$m, the RMS-error to $0.72\,\mu$m. The patient achieved a best spectactle corrected visual acuity (BSCVA) of 20/40. On the left hand side of Fig. 1.26 the appearance of the Wavescan$^{\mathrm{TM}}$-tunnel-target is blurred correspondingly. In Fig. 1.27, the compensated wavefront and the target image are depicted. By closed loop adaptive optical control the RMS-error can be reduced to $0.07\,\mu$m, corresponding to one tenth of a wavelength of light. The Wavescan$^{\mathrm{TM}}$-tunnel target image is sharpened accordingly. Indeed, the patient's vision was improved by a therapeutic custom ablation procedure to nearly perfect 20/12.5 performance.

1.9 Summary

It was shown, that the introduction of wavefront–technology into ophthalmology allows to determine all optical aberrations of the human eye, far beyond the spherocylindrical refractive error. Based on WaveScan$^{\mathrm{TM}}$-technology the reproducibility and accuracy of the new technique was established in worldwide multicenter clinical studies. It was demonstrated that closed loop adaptive optical control allows for improved spatial resolution of aberration measurements, increasing the resolution limit by two orders of magnitude over e.g.

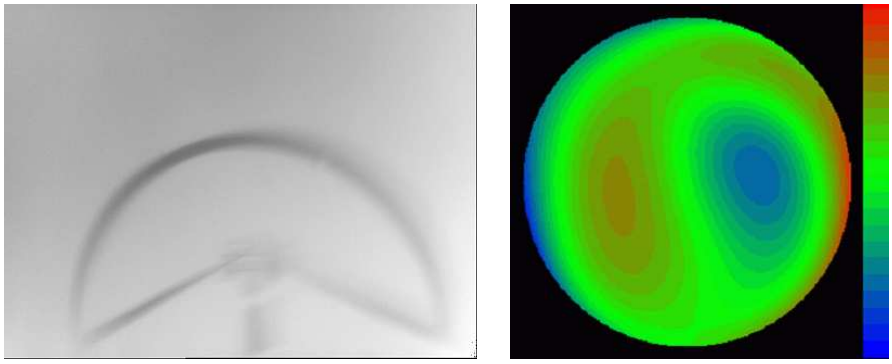

Fig. 1.26. Waveplate simulating human eye with high coma. Left: defocused image, right: uncompensated wavefront

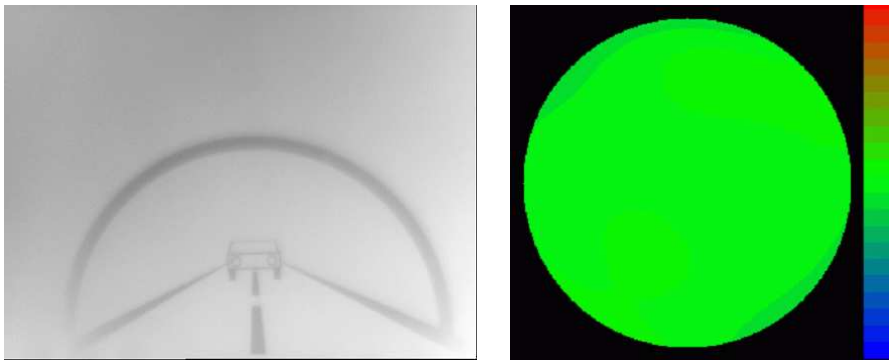

Fig. 1.27. Compensation of high coma aberration. Left: Focused image, right: compensated wavefront

Hartmann-Shack technologies. In addition, adaptive optical stimulus generation can be used for preoperative simulation of refractive outcomes. Based on highly integrated micro-optoelectronic devices a new diagnostic instrument was developed, the so-called CLAO/BILLE-Aberrometer. The safety and efficiency of custom ablations based on WaveScan^{TM}-measurements was established in first controlled clinical studies.

References

1. J.F. Bille, K. Freischlad, G. Jahn, F. Merkle: *Image restauration by adaptive-optical phase compensation.* Proceedings "6th International Conference on Pattern Recognition", Munich, Germany, Oct. 19-22, 1982
2. J.F. Bille: *Method and Apparatus for Forming an Image of the Ocular Fundus*, U.S. Patent 4, 579, 430 (April 1, 1986)

3. J.F. Bille, G. Jahn, M. Frieben: *Modal control for wavefront reconstruction in adaptive optics*, SPIE **332** Advanced Technology Optical Telescopes, 269 (1982)
4. J.F. Bille, B. Grimm, J. Liang, K. Mueller: *Imaging of the retina by scanning laser tomography*, New Methods in Microscopy and Low Light Imaging, SPIE **1161**, 417 (1989)
5. J. Liang: *A new method to precisely measure the Wave Aberrations of the Human Eye with a Hartmann-Shack Sensor*. Dissertation, Ruprecht-Karls-Univeristt, Heidelberg 1991
6. J. Liang, B. Grimm, S. Goelz, J.F. Bille: *Objective measurement of wave aberrations of the human eye with the use of a Hartmann-Shack wavefront sensor*, JOSA A, No.7, 1949 (1994)
7. E.S. Claflin and N. Baraket: *Configuring on electrostatic membrane mirror by least-squares fitting with analytically derived influence functions*, JOSA A **3**, 1833 (1986)
8. A.W. Dreher, J.F. Bille, and R.N. Weinreb: *Active optical depth improvement of the laser tomographic scanner*, Applied Optics, **28**, 804 (1989)
9. M. Kasper, D. Looze, S. Hippler, T. Herbst, A. Glindemann, T. Ott, A. Wirth: *ALFA: Adaptive Optics Calar Alto Observatory-Optics, Control System, and Performance*, Experimental Astronomy **10**, 49 (2000)
10. G.V. Vdouin: *Adaptive mirror micro machined in silicon PhD thesis, University of Delft*, Netherlands, 1997
11. J.F. Bille: *Method for Programming an Active Mirror to Mimic a Wavefront* , U.S. Patent 6, 220, 707 B1 (April 24, 2001)
12. D. Droste and J.F. Bille: *An ASIC for Hartmann-Shack Wavefront Detection* IEEE Journal of Solid-State Circuits (2002)
13. U. von Pape: *Wavefront sensing in the human eye PhD* Dissertation, University of Heidelberg, (2002)
14. R. Ragazzoni: *Pupil plane wavefront sensing with an oscillating prism* J. Mod. Opt., **43**, 289 (1996)
15. S. Wühl: Diploma Thesis, University of Heidelberg, (2000)
16. F. Müller: Dissertation, University of Heidelberg, (2001)

2 Optical Quality of the Human Eye: The Quest for Perfect Vision

J.F. Bille, J. Büchler Costa, and F. Müller

2.1 Introduction

The optical errors caused by the elements of the optical apparatus of the eye, as the cornea or the lens, strongly degrade the image on the retina.

The correction of the lower orders, as tilt, defocus and astigmatismus, through spectacles or contact lenses, is normally prescribed by the doctor.

With a pupil of circa 3 mm , which is usual at normal daylight, the best compromise between the pupil size and the aberrations is achieved. If the pupil size is smaller, diffraction strongly limits the visual performance, while for bigger pupils the image transmission is heavily prejudiced by the aberrations in the margins. In Fig. 2.1, point spread function (PSF) for different pupil size are shown. The corresponding modulation transfer function (MTF) are demonstrated in Fig. 2.2.

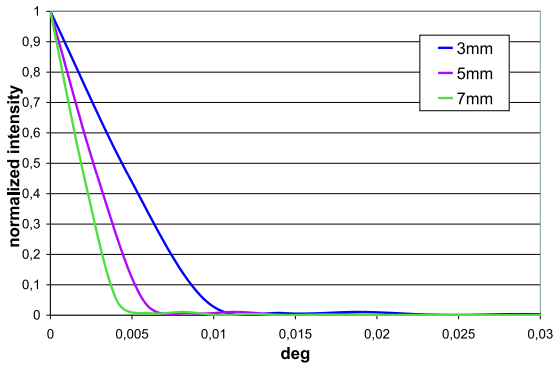

Fig. 2.1. PSFs for diameter 3, 5 and 7 *mm*

2.2 The Quality of the Human Eye

Most people experience in daily life the limited quality of the eye, caused by the elements of the optical apparatus, as the cornea or the lens, which

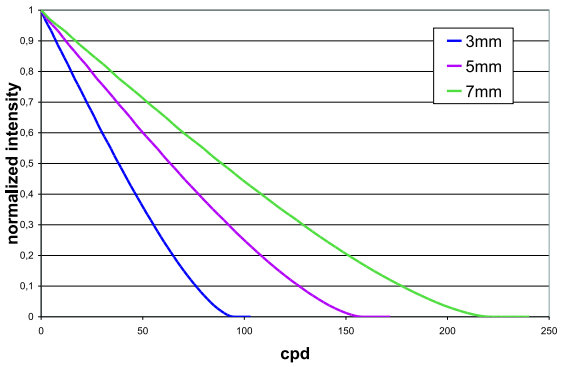

Fig. 2.2. MTFs for diameter 3, 5 and 7 *mm*

strongly degrade the image on the retina. The correction of the lower orders, as tilt, defocus and astigmatismus, the simplest optical errors, is normally prescribed by the doctor, through spectacles or contact lenses. But with a pupil of circa 3 mm, which is usual at normal daylight, the best compromise between the pupil size and the aberrations is achieved. If the pupil size is smaller, diffraction strongly limits the visual performance, while for bigger pupils the image transmission is heavily prejudiced by the aberrations in the margins, like the spherical aberration, for example. A natural measure of

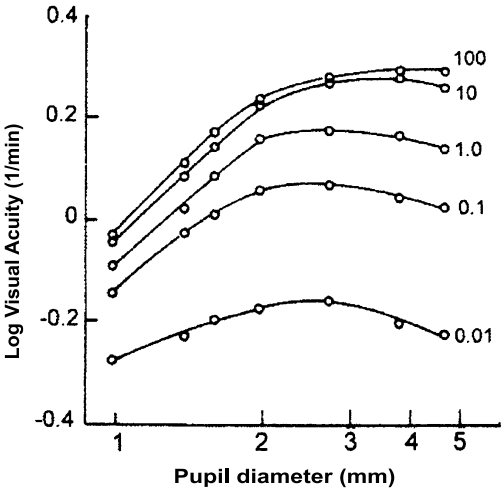

Fig. 2.3. Visual acuity vs. pupil size at different illuminations [3]. The optimum visual acuity is achieved for 2-3 mm pupil diameter

quality of the human eye is its ability to see fine detail, its *visual acuity*. It is the spatial resolving capacity of the visual system. There are various ways to measure and specify visual acuity. Usually a proband has to read letters of a specific size or has to determine the orientation of special test characters. The most prominent test characters used are Snellen letters (normally E) and Landolt Cs. Later we will use these kind of vision charts to simulate retinal images under various conditions.

The visual acuity of a perfect eye is limited by diffraction and ultimately by the photoreceptor density of the eye. Thus the acuity of the eye should theoretically improve with larger pupils until the size of the point spread function, the intensity pattern of a transmitted luminous point (see next chapter for mathematical definition), reaches the dimension of single rods. As shown in Fig. 2.3 this is not the case: as the pupil gets larger, visual acuity increases until it reaches its optimum value. At larger pupils optical aberrations prevail and so the measured acuity diminishes. The measurement of wavefront errors explains this findings. In Fig. 2.4 the reaction of the wavefront Root Mean Square deviation (RMS) to a change in pupil diameter is shown for two sample eyes. The rms value increases steadily with larger pupil size. This

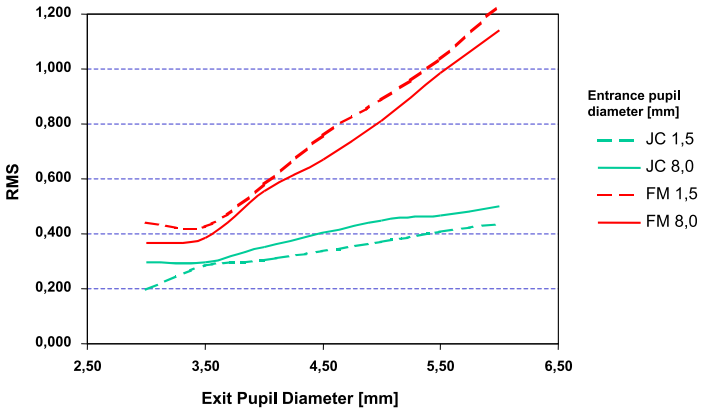

Fig. 2.4. Variation of wavefront rms with pupil size

does not contradict Fig. 2.3 because—in spite of this increase—the resolution limit due to diffraction declines.

At larger pupil sizes the Strehl ratio, normalized maximum of the point spread function, assumes values of some percent and ceases to be a useful measure of optical quality because the associated point spread function takes a complex shape with many singular maxima.

As one can see, the change is strongly dependent on the particular proband, as is the actual shape of the aberrations [5,9].Thus it is of no use to

apply a generic correction of high order aberrations but it is necessary to correct each patient individually.

2.3 Linear Systems

For the description of the optical quality of the human eye some mathematical background is necessary. First we make the assumption that the eye is a linear transmission media. Taking f as the incoming signal and g as the outgoing signal, we can describe the effect of the system as a linear operator $\mathcal{L}$

$$f(x,y) \mapsto g(X,Y) \quad \Rightarrow \quad g(X,Y) = \mathcal{L}\{f(x,y)\} \tag{2.1}$$

This allows us to determine a system response function to a δ-signal, which is called the *Point Spread Function* (PSF) of the system.

If we know the transmission function of a point source, we can decompose the incoming signal in many point sources and sum the corresponding outgoing signals. Mathematically this is described by:

$$g(X,Y) \quad = \int_{-\infty}^{\infty}\int_{-\infty}^{\infty} f(x,y)\,\mathrm{PSF}(X-x, Y-y)\,dx\,dy \tag{2.2}$$

or shorter: $g = f \otimes \mathrm{PSF}$, what is called a convolution.

Another important parameter for the description of the optical quality is the *Optical Transfer Function* (OTF), which is the Fourier Transform of the PSF. It contains the information about the effect of the system in the frequency space. As example see Fig. 2.5 and Fig. 2.6

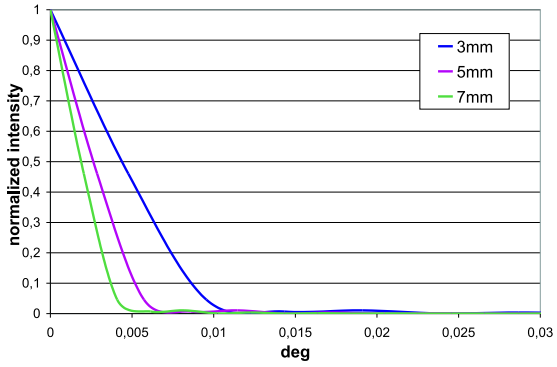

Fig. 2.5. PSFs for diameter 3, 5 and 7 mm without aberrations

The *Strehl ratio* is defined as the ratio between maximum intensity of an image of a point source and maximum intensity of the same source imaged with an ideal optical system.

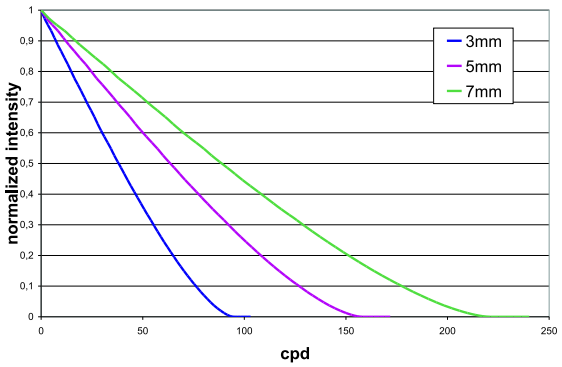

Fig. 2.6. Modulation Transfer Functions (modulus of the OTF) for diameter 3, 5 and 7 mm without aberrations

2.3.1 Optical Systems

Diffraction Limited Systems These systems transform incoming divergent spherical waves in outgoing convergent perfectly spherical waves. They converge to an almost ideal point, which is the center of the airy-disk (see Fig. 2.7). The only limiting factor for the imaging quality is the diffraction caused by the edges of the pupil. This causes the enlargement of the ideal point to a broader circle.

To explain the possible optical resolution of an optical system it is necessary to skip to waveoptics. Geometrically a smaller pupil would always generate a smaller point on the retina. However, below a certain aperture size, the point gets wider, because of the scattering at the pupil edges, what is well described by Fraunhofer diffraction. A circular pupil images a point as a pattern of concentric bright and dark rings, as shown in Fig. 2.7. The bright circular center is called the airy-disk, and its half angular dimension is given by:

$$\theta = 1.22\,\frac{\lambda}{\mathrm{d}}, \tag{2.3}$$

where d is the pupil diameter and λ is the wavelength of the light.

This determines the maximum resolution of the eye, because two points can only be distinguished if the sum of the intensities of both irradiated surfaces shows clearly two maxima. Using the Rayleigh criterion this happens when the maximum of one disk falls on the first minimum of the other pattern. The angular distance is then given by 2.3.
According to this criterion the eye could, if it was a diffraction limited system, resolve approximately 47 seconds of arc with a pupil diameter of 3 mm and with light of wavelenght 555 nm, with a diameter of 4 mm it should resolve 35 seconds of arc.

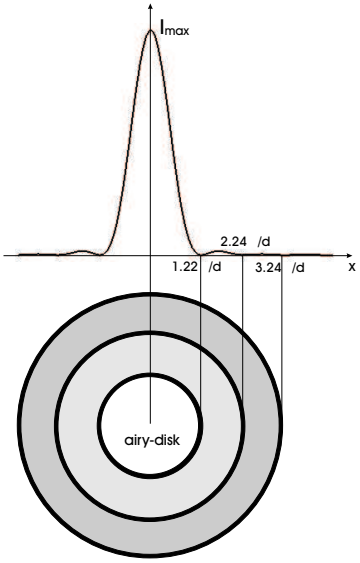

Fig. 2.7. Intensity distribution of the diffraction pattern with a circular pupil. The position of the minima is given

Systems with Aberrations The waves that come out of this systems differ clearly from a spherical wave and the cause are the optical aberrations. These are normally more or less regular differences that the real system or its optical components have from the ideal system. There is for example the existence of different indices of refraction in the center and the edges of the pupil, what is called spherical aberration.

The Photoreceptor Sampling of the Retina One of the factors that can limit visual acuity is also the size and the density of the photoreceptors on the retina. In the fovea the cone density is estimated to be 147.000 per square millimeter (Osterberg 1935) and the center to center spacing between 2 and 3 μm. We assume they are approximately hexagonal and packed as shown in Fig. 2.8. Applying the Nyquist sampling theorem, the maximum frequency

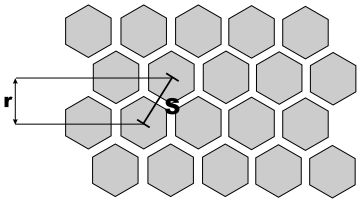

Fig. 2.8. Photoreceptor sampling

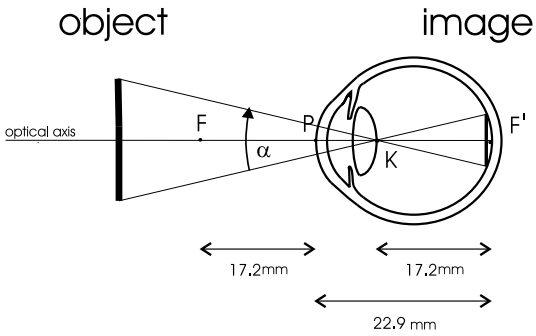

Fig. 2.9. Reduced eye from Listing

that can be clearly distinguished by this distribution is half of the reciprocal of the distance between the receptor rows. So this limit is

$$f_N = \left(\sqrt{3}S\right)^{-1}, \tag{2.4}$$

where S is the center to center spacing. Using the model of the reduced eye from Listing (see Fig. 2.9), with $S = 2.5\,\mu m$ we get $f_N = 69\,cpd$ (cycles per degree).

The detection of the position of the spacing in a Landolt C, for example, should be possible if the spacing has 0.4 to 0.5 minutes of arc (corresponding to Vision 2.3 or almost 20/8). Beyond this frequency aliasing in the detection is expected [11].

Modulation Threshold The Modulation Threshold function (which is the reciprocal of the Contrast Sensitivity function) is defined as being the minimum required contrast of a sinusoidal light signal for the eye to detect the illumination variance at every frequency. Normally it is measured by presenting targets to patients at various contrast levels.

Optical systems are very well described by the Linear Systems Theory. In case of coherent light the system is linear in the amplitude, in our case, with incoherent illumination, it is linear in the intensity. Then we have:

$$I_i(X,Y) \;=\; \int_{-\infty}^{\infty}\int_{-\infty}^{\infty} I_0(x,y)\,\mathrm{PSF}(X-x,Y-y)\,dx\,dy, \tag{2.5}$$

where I_i is the image intensity and I_0 is the object intensity (see 2.2). To keep it simple, we take the magnification factor as being 1.

The PSF washes out the image, since sharp lines or points are broadened, and the resolution diminishes.

In frequency space the OTF is used instead of the PSF. As intensities are real non-negative quantities, the spectrum has its maximum, which is not 0, at frequency 0. Normally the spectra are normalised, the fourier transform

of the intensities are divided by the 0-frequency value. This value can be interpreted as the underground, in case of black and white bars medium-grey. This allows us to interpret the OTF as the level of contrast of each frequency term, taking values from 0 to 1.

As the OTF is a complex function, it is possible to write it in exponential form:

$$\mathrm{OTF} = (\mathrm{MTF})\, e^{i(\mathrm{PTF})}. \tag{2.6}$$

Contrast Measurements One very important skill of the eye is the capability of recognizing patterns even if they have little contrast and are not well illuminated. Contrast (M) is defined as

$$\mathrm{M} = \frac{\mathrm{I_{max}} - \mathrm{I_{min}}}{\mathrm{I_{max}} + \mathrm{I_{min}}}. \tag{2.7}$$

The contrast attenuation factor at every spatial frequency gives us the OTF , which describes the optical properties of the system. With the Hartmann-Shack Wavefront measurements we have an objective method to determine this function.

Frequency is normally given in *cpd*. A sinusoidal black and white pattern with a frequency of 30 cpd corresponds to a resolution of 1 minute of arc or Vision 20/20.

2.4 Representation of Aberrations

Classically, only two kinds of optical aberrations are corrected by the oculist: sphere and cylinder. Let's first regard these refractive errors. If the eye has too much or too less optical power in relation to its length, one speaks of myopia respectively of hyperopia. Usually the eye is too long (myopia) or too short (hyperopia). The optical path of light rays entering the eye is pictured in Fig. 2.4. The third well known aberration is cylinder or astigmatism. There the power of the refracting system of the eye is higher in one meridian than in the other. Thus the entering light is not focused to a point but to two perpendicular lines in different depths [1]. Higher order, that is more complicated aberrations are all summarized as *irregular astigmatism*. If this defect is strong it is corrected by a hard contact lens.

The classical aberrations are described as an error in focal power, in the case of sphere the absolute error of power, in the case of astigmatism the difference between the focal powers of the meridians. Consequently the unit *diopter* is used. Almost always the power of the necessary correction lens is

[1] Greek stigma ($\sigma\tau\acute{\iota}\gamma\mu\alpha$) means point. Thus the term *a-stigma-tism* means: absence of a focal point

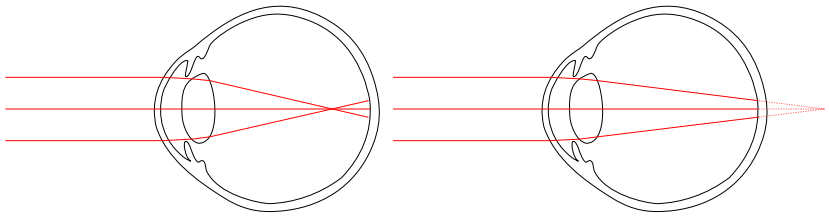

Fig. 2.10. Classical refraction errors

indicated. In the clinical practice there is so far no standard way to characterize irregular astigmatism. This is the consequence of the lack of capability to correct these errors.

In vision science it is common to represent the errors of the eye as wavefront aberrations. As shown in Fig. 2.4, wavefronts are surfaces that are perpendicular to light rays. The figure shows an example of light entering the human eye. Such as the sheaf of parallel rays is refracted to a converging bundle, the formerly flat wavefront is transformed to a converging spherical wavefront . In the sense of electrodynamic theory the wavefront is a *surface of same phase* (see Fig. 2.4). This corresponds to the location where all light is which started at the same point of time, provided that the intermediate media are free of dispersion [2].

There are various kinds of mathematical representation of wavefronts. For a useful representation it is essential that the chosen set of function allows to compute the classical aberrations easily. Polynomials are well suited for this purpose and are usually used to characterize the wavefront shape. Among polynomials the most frequently used function sets in optical shop

[2] The speed of light is the same for all wavelengths

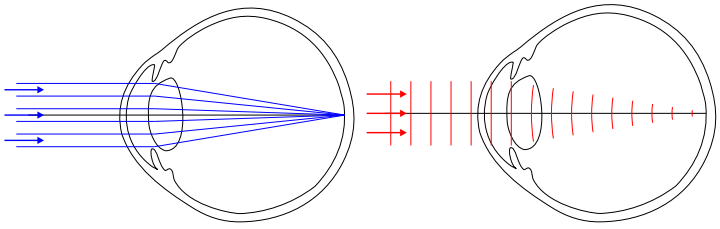

Fig. 2.11. Different representations of light entering an ideal eye. For simplification all light is refracted in one plane

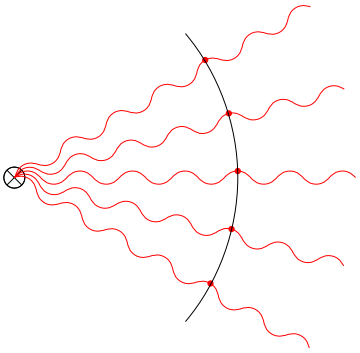

Fig. 2.12. Electromagnetic waves escaping a source of light. The points of same phase form a wavefront

Table 2.1. Zernike polynomials up to 4th radial order. Notation as recommended in [8]

Term	Polar representation	Monomial representation	Name
Z_0^0	1	1	Constant
Z_1^{-1}	$\rho \sin\theta$	x	Tilt in y
Z_1^1	$\rho \cos\theta$	y	Tilt in x
Z_2^{-2}	$\rho^2 \sin 2\theta$	$2xy$	Astigmatism ± 45
Z_2^0	$2\rho^2 - 1$	$2x^2 + 2y^2 - 1$	Defocus
Z_2^2	$\rho^2 \cos 2\theta$	$y^2 - x^2$	Astigmatism 0/90
Z_3^{-3}	$\rho^3 \sin 3\theta$	$3xy^2 - x^3$	
Z_3^{-1}	$(3\rho^3 - 2\rho)\sin\theta$	$-2x + 3xy^2 + 3x^3$	Coma in x
Z_3^1	$(3\rho^3 - 2\rho)\cos\theta$	$-2y + 3x^2y + 3y^3$	Coma in y
Z_3^3	$\rho^3 \cos 3\theta$	$y^3 - 3x^2y$	
Z_4^{-4}	$\rho^4 \sin 4\theta$	$4y^3x - 4x^3y$	
Z_4^{-2}	$(4\rho^4 - 3\rho^2)\sin 2\theta$	$-6xy + 8y^3x + 8x^3y$	
Z_4^0	$6\rho^4 - 6\rho^2 + 1$	$1 - 6y^2 - 6x^2 + 6y^4 + 12x^2y^2 + 6x^4$	3rd order spherical aberr.
Z_4^2	$(4\rho^4 - 3\rho^2)\cos 2\theta$	$-3y^2 + 3x^2 + 4y^4 - 4x^4$	
Z_4^4	$\rho^4 \cos 4\theta$	$y^4 - 6x^2y^2 + 4x^4$	

testing include Seidel polynomials and Zernike polynomials [12,10]. Lately Zernike polynomials have found most attention in vision science [4,5,7]. In table 2.1 the 14 Zernike polynomials of lowest order are given. As one can see, Z_2^0 corresponds to defocus whilst Z_2^{-2} and Z_2^2 correspond to astigmatism. Other well known optical aberrations have their correspondence in Zernike polynomials as well, e.g. Z_{12} represents 3rd order spherical aberration. Table 2.2 shows pseudo-3D graphics of these functions.

Table 2.2. Zernike polynomials up to 4th order

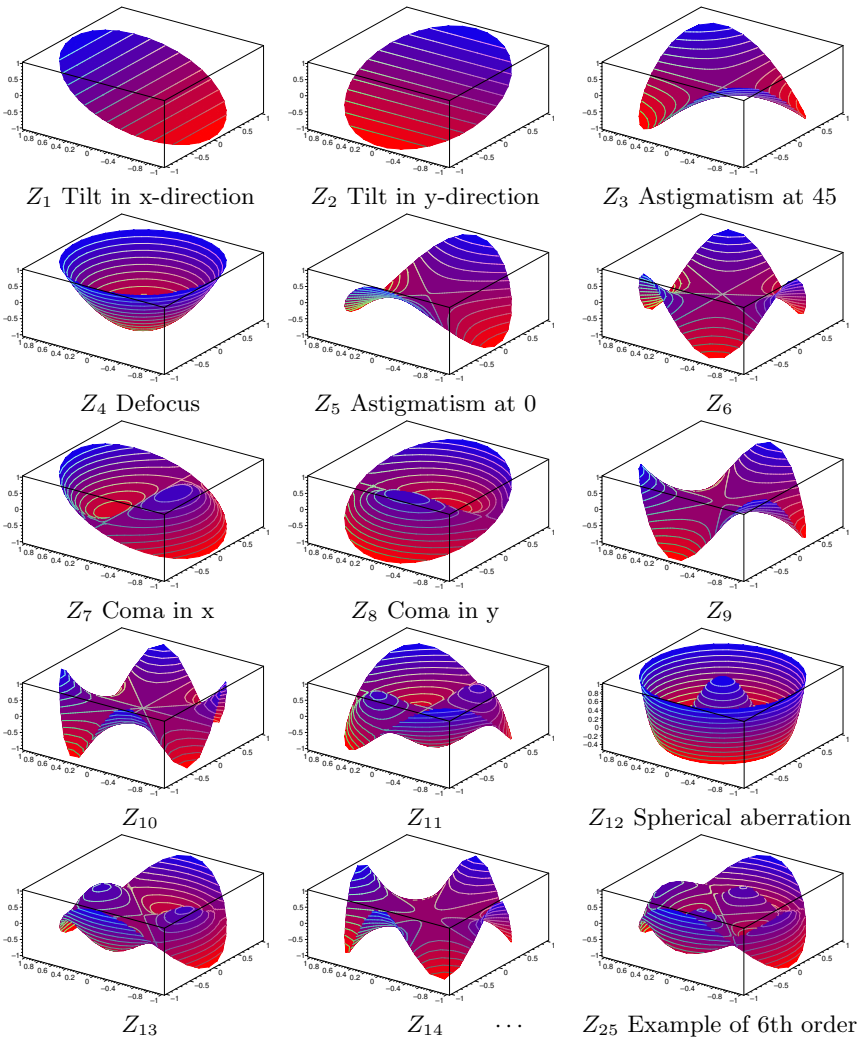

With the wavefront, the optical properties of the system in question are known. For example the *Strehl ratio* can be determined. The peak to valley value Γ of the wavefront is sufficient to estimate the minimum Strehl ratio. For a given $\Gamma < \lambda$ the minimum Strehl ratio i is [2]:

$$i = 0.5(cos\frac{2\pi\Gamma}{\lambda} + 1) \tag{2.8}$$

An even better estimate of the Strehl ratio can be done using the wavefront root-mean-square deviation from the mean σ. It can be shown [6] that for

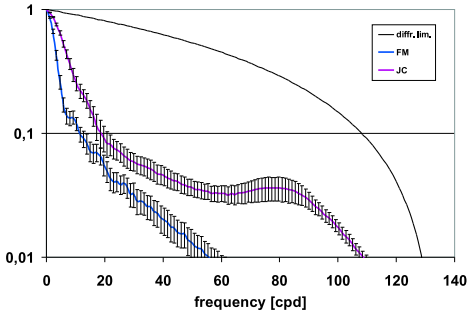

Fig. 2.13. Modulation transfer function based on measurements on two eyes. Pupil-diameter is in both cases 6 mm

small aberrations the Strehl ratio is:

$$i \approx \left(1 - 2\pi^2 \left(\frac{\sigma}{\lambda}\right)^2\right)^2 \tag{2.9}$$

Thus for small aberrations [3] the Strehl ratio depends only on the (root) mean square of the wavefront, not on the specific shape of the particular aberration.

As an example we present plots from typical MTFs measured on two eyes (Fig. 2.13) and a 3-dimensional representation of a PSF also from a patients eye (Fig. 2.14).

2.5 Simulations

The Snellen Es have one disadvantage: because of the strong grey ramp of the letter, its direction can still be estimated from when the single lines

[3] not much larger than $\frac{\lambda}{10}$

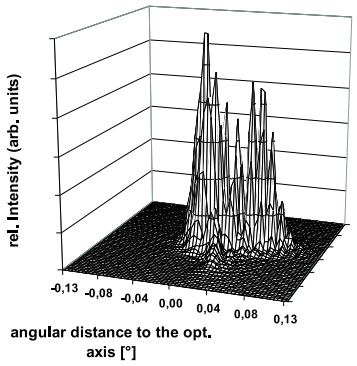

Fig. 2.14. Point spread function based on measurements on a patients eye. Pupil-diameter is 6 mm

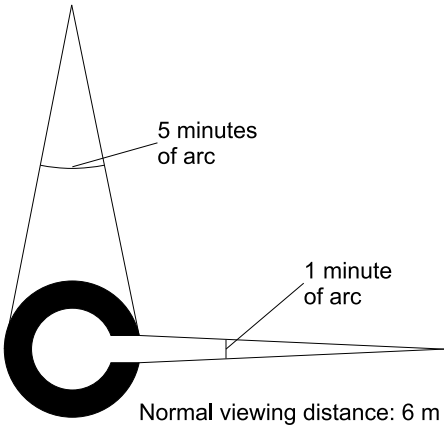

Fig. 2.15. Construction of a Landolt C for testing 20/20 visual acuity

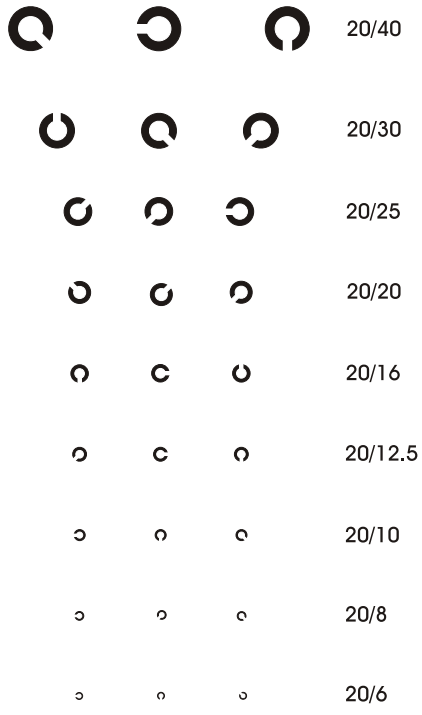

Fig. 2.16. Unaberrated Vision Chart

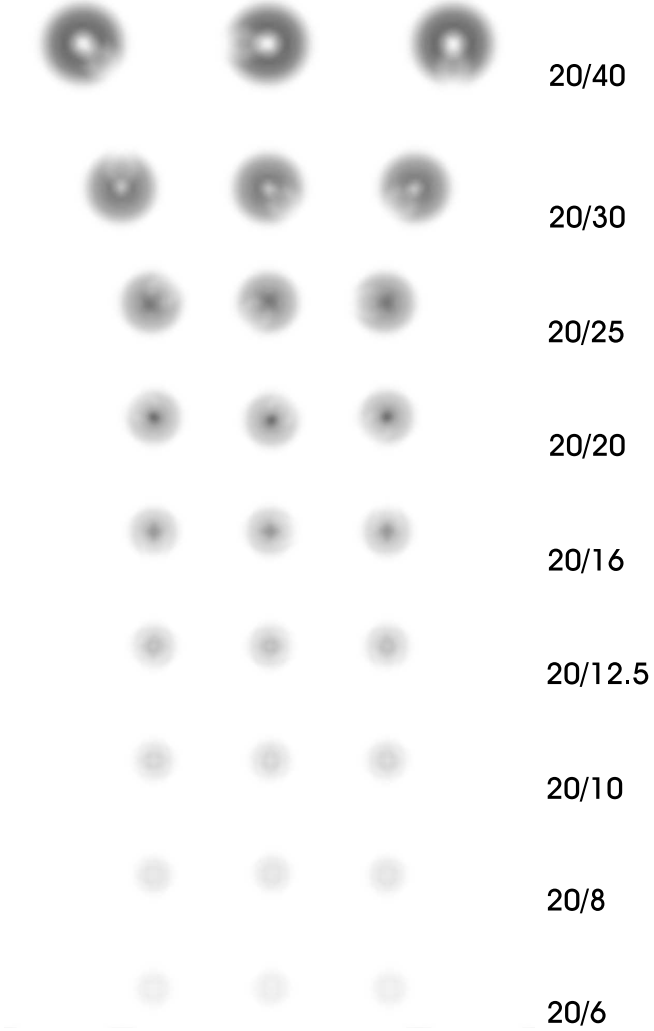

Fig. 2.17. Vision Chart for 0.5 diopters defocus (without Styles-Crawford effect)

are already blurred. This is the reason that we used Landolt charts in the simulations of the following chapters.

We used a vision chart with Landolt rings as optotypes (see Fig. 2.5), where the width of the gap and the line is a fifth of the symbol size. For the lines corresponding to visual acuity of 0.5 to 1.0 the horizontal and vertical spacing between the symbols is twice the size of the optotypes and for the lines for testing visual acuity better than 1.0 the spacing is 15 arcminutes. Since our interest lays on the normal and supernormal acuity, our vision chart has its main focus on these chart lines (see Fig. 2.16).

This vision chart has been convolved with different Point Spread Functions of predetermined aberrations or patient eyes, so that the outcome represents the image of the chart as it is projected on the retina.

We then simulated the correction with different segmented active mirrors, where the submirror size, the gap-size and gap-reflectivity, an estimated submirror curvature and some amplitude of noise in the submirror height could be accounted for. The used parameters correspond to the measured characteristics and the given specifications of the manufacturer. The first simulation (see Fig. 2.17) shows the effect of half a diopter of defocus on the quality of the image transmission through the optical apparatus of the eye.

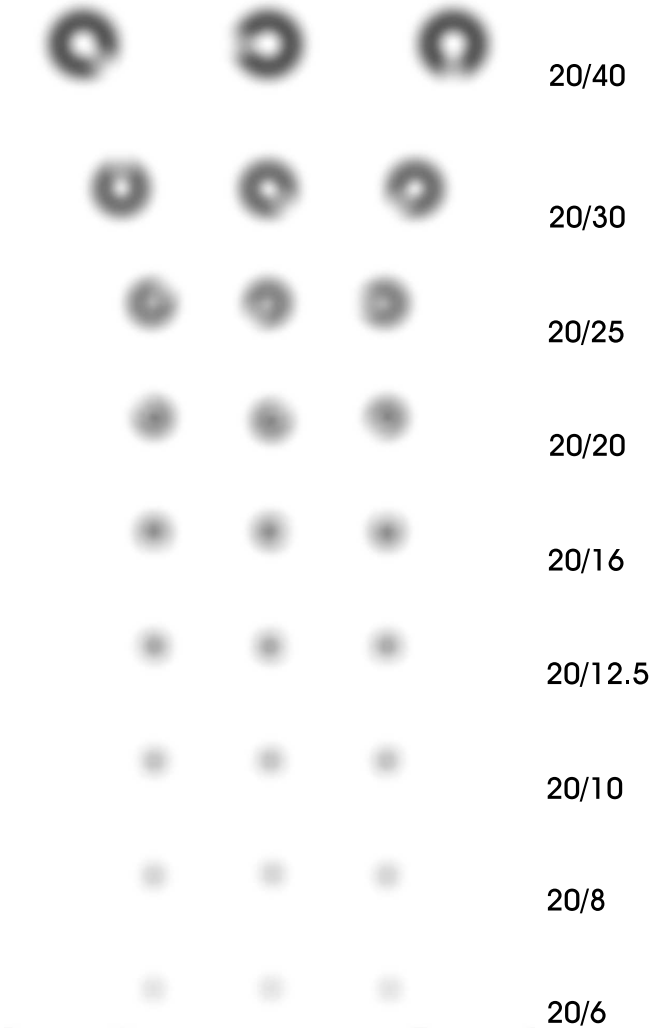

Fig. 2.18. Vision Chart for 0.5 diopters defocus (with Styles-Crawford effect)

In Fig. 2.18 a simulation of the Styles-Crawford effect of the first kind on the previous chart is shown. This effect has its origin in the waveguide nature of the photoreceptors, so that light passing through the center of the pupil is perceived brighter than light passing through the edges. It can be modeled as a filter, which is placed in front of the pupil with an exponential form: $exp(-p_e R^2)$, where R is the distance from the center and p_e is a coefficient between 0.1 and 0.2 (see [1] for details). Note that the image turned sharper and the phenomenon of contrast inversion occurs at smaller Vision Acuity. In the following simulations this effect was taken into account.

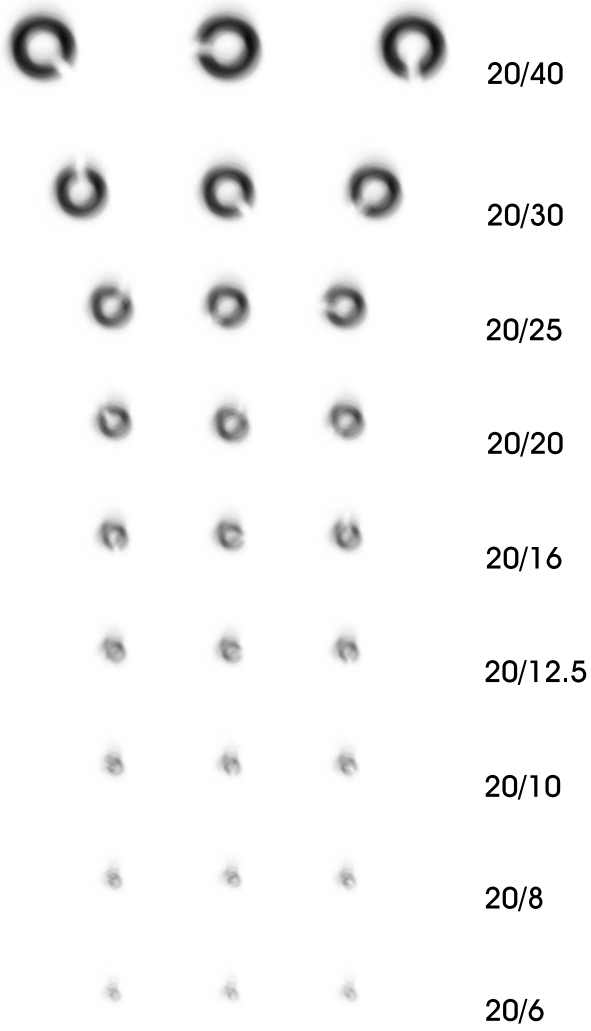

Fig. 2.19. Vision Chart for a 20/10 eye (with Styles-Crawford effect)

Fig. 2.19 shows the vision chart as it is projected on the retina of a 20/10 eye-patient, whose aberrations were previously determined.

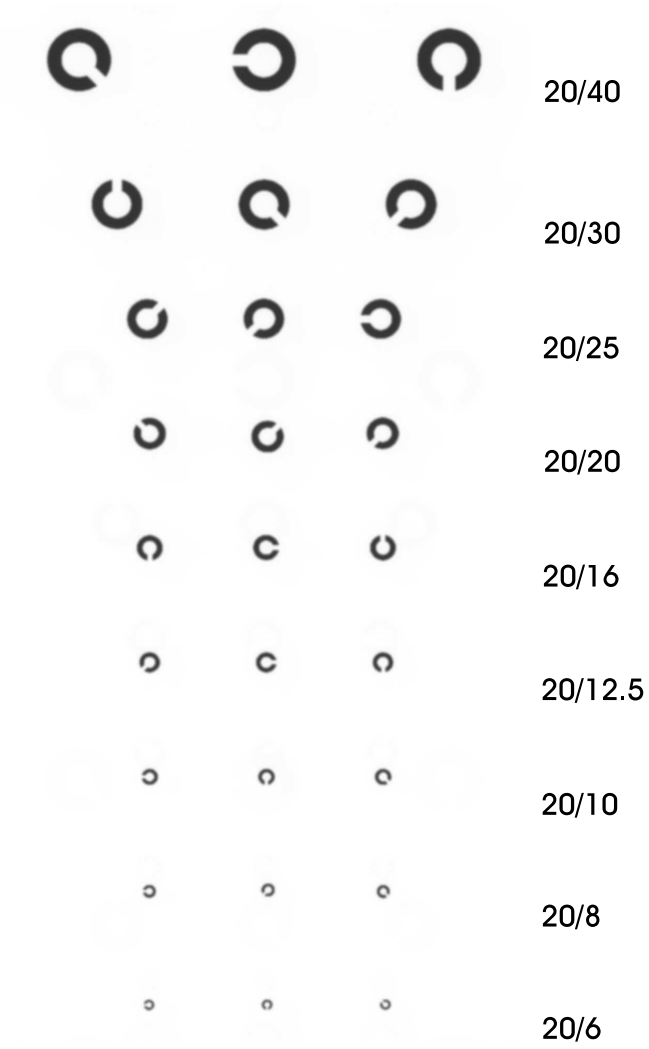

Fig. 2.20. Vision Chart for a 20/10 eye (with Styles-Crawford effect) corrected with a segmented active mirror. The mirror parameters were mirrorsize 37 μ m, width of the arms 3 μ m, noise in the stroke amplitude 30 nm and a PV of also 30 nm per submirror

In Fig. 2.20 we can see the same eye but now after simulating a correction with a segmented active mirror, using the measured characteristics and parameters specified by the manufacturer.

Fig. 2.21. Vision Chart for a 20/20 eye (with Styles-Crawford effect)

The next chart, Fig. 2.21, shows the image for a 20/20 eye, an eye with normal (100%) vision. We notice how degraded the projection on its retina is. It is important to keep in mind, that the neuronal processing of the image can correct for the double images, with the knowledge of the pattern to be recognised, and can still distinguish the position of the gap, until it is optically impossible.

Fig. 2.22. Vision Chart for a strong aberrated eye (with Styles-Crawford effect)

In Fig. 2.22 we used the parameters of a patient with a strongly aberrated eye, which had been submited to refractive surgery. The eye was misaligned during the procedure resulting in a dramatic degradation of the transmitted image. In the next chart, Fig. 2.23, we see the correction of the aberrations of this eye, with the same mirror parameters as before in Fig. 2.20. The result is a sharp image, allowing great increase in visual acuity.

Fig. 2.23. Vision Chart for a strong comatic eye (with Styles-Crawford effect) after correction with a segmented mirror (see legend from Fig. 2.20)

References

1. D. A. Atchison, A. Joblin, G. Smith Influence of Styles-Crawford effect apodization on spatial visual performance. J. Opt. Soc. Am A. **15**, No.9, 2545 (1998)
2. A. van den Bos Aberration and Strehl Ratio. J. Opt. Soc. Am A **17**, No.2, 356 (2000)
3. W. N. Charman Visual Optics and Instrumentation. Volume 1 of *Vision and Visual Dysfunction*. first edition. (1991)
4. J. Liang, B. Grimm, S. Goelz, J. Bille Objective measurements of the wave aberrations of the human eye with a Hartman-Shack wavefront sensor. J. Opt. Soc. Am A **11**, 1949 (1994)
5. J. Liang, D. R. Williams Aberrations and retinal image quality of the normal human eye. J. Opt. Soc. Am A **14**, 2873 (1997)

6. A. Maréchal Étude des effets combins de la diffraction et des aberrations gomtriques sur limage dun point lumineux. Rev. Opt. Thorique Instrum. **26**, 257 (1947)
7. P. M. Prieto, F. Vargas-Martín, S. Goelz, P. Artal Analysis of the performance of the Hartmann-Shack sensor in the human eye. J. Opt. Soc. Am A **17**, No.8, 1388 (1997)
8. L. N. Thibos, R. A. Applegate, J. T. Schwiegerling, R. Webb et al. Standards for Reporting the optical Aberrations of Eyes. in *Vision Science and Its Applications*. Opt. Soc. Am. Technical Digest. Opt. Soc. Am. 146–149 (2000)
9. G. Walsh, W. N. Charman, H. C. Howland Objective technique for the determination of monochromatic aberrations of the human eye. J. Opt. Soc. Am. A **1**, No.9, 987 (1984)
10. J. Y. Wang, D.E. Silva Wave-front interpretation with Zernike polynomials. Appl. Opt. **19**, No.9, 1510 (1980)
11. D. R. Williams Aliasing in human foveal vision. Vision Res. **25**, 195 (1985)
12. F. Zernike Beugungstheorie des Schneidenverfahrens und seiner verbesserten Form, der Phasenkontrastmethode. Physica. **94**, 689 (1934)